

12-22-2011

Linear-Quadratic Control of a MEMS Micromirror Using Kalman Filtering

Jamie P. Schnapp

Follow this and additional works at: <https://scholar.afit.edu/etd>

Part of the [Electrical and Electronics Commons](#)

Recommended Citation

Schnapp, Jamie P, "Linear-Quadratic Control of a MEMS Micromirror Using Kalman Filtering" (2011). *Theses and Dissertations*. 1154.
<https://scholar.afit.edu/etd/1154>

This Thesis is brought to you for free and open access by the Student Graduate Works at AFIT Scholar. It has been accepted for inclusion in Theses and Dissertations by an authorized administrator of AFIT Scholar. For more information, please contact richard.mansfield@afit.edu.



**LINEAR-QUADRATIC CONTROL OF A MEMS MICROMIRROR USING
KALMAN FILTERING**

THESIS

Jamie P. Schnapp, Capt, USAF

AFIT/GE/ENG/11-44

**DEPARTMENT OF THE AIR FORCE
AIR UNIVERSITY**

AIR FORCE INSTITUTE OF TECHNOLOGY

Wright-Patterson Air Force Base, Ohio

APPROVED FOR PUBLIC RELEASE; DISTRIBUTION UNLIMITED

The views expressed in this thesis are those of the author and do not reflect the official policy or position of the United States Air Force, Department of Defense, or the U.S. Government.

This material is declared a work of the U.S. Government and is not subject to copyright protection in the United States.

AFIT/GE/ENG/11-44

**LINEAR-QUADRATIC CONTROL OF A MEMS MICROMIRROR USING
KALMAN FILTERING**

THESIS

Presented to the Faculty

Department of Electrical Engineering

Graduate School of Engineering and Management

Air Force Institute of Technology

Air University

Air Education and Training Command

In Partial Fulfillment of the Requirements for the
Degree of Master of Science in Electrical Engineering

Jamie P. Schnapp, BS

Capt, USAF

December 2011

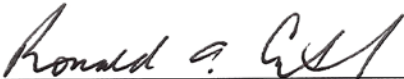
APPROVED FOR PUBLIC RELEASE; DISTRIBUTION UNLIMITED

**LINEAR-QUADRATIC CONTROL OF A MEMS MICROMIRROR USING
KALMAN FILTERING**

Jamie P. Schnapp, BS

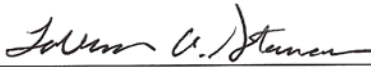
Capt, USAF

Approved:




Dr. Ronald A. Coutu, Jr., P.E., USAF (Chairman)

23 Nov 11
Date



Lt Col LaVern A. Starman, Ph.D., USAF (Member)

23 Nov 2011
Date



Maj Kenneth A. Fisher, Ph.D., USAF (Member)

23 Nov 2011
Date

Abstract

The deflection limitations of electrostatic flexure-beam actuators are well known [64]. Specifically, as the beam is actuated and the gap traversed, the restoring force necessary for equilibrium increases proportionally with the displacement to first order, while the electrostatic actuating force increases with the square of the potential difference across the gap, as well as the inverse square of the gap. Equilibrium, and thus stable open-loop voltage control, ceases at one-third the total gap distance, leading to an unstable actuator snap-in. A Kalman Filter is designed with an appropriately complex state dynamics model to estimate actuator deflection accurately given voltage input and capacitance measurements, which are then used by a Linear Quadratic controller to generate a closed-loop voltage control signal. The constraints of the latter are designed to maximize stable control over the entire gap. The design and simulation of the Kalman Filter and controller are presented and discussed, with static and dynamic responses analyzed, as applied to basic, 100 μm by 100 μm square, flexure-beam-actuated micromirrors fabricated by PolyMUMPs. Successful application of these techniques enables demonstration of smooth, stable deflections of 50% and 75% of the gap.

Acknowledgments

First and foremost, I'd like to convey my sincerest gratitude for the guidance, insight, support, and patience shown to me by Lt Col Lavern Starman and Dr. Ron Coutu. I'd also like to sincerely thank Mr. Mike Camden of AFRL/VACC and Dr. Tom Nelson of AFRL/RYPD and respective division leadership for their support and gracious latitude during this endeavor. In particular, I'd like to thank Dr. Matt Grupen of RYPD for his patiently explaining the philosophical nature of capacitance and entertaining other random science questions. Last but not least, I'd like to thank my wife, whose inspiration and support in this effort was unequivocally essential.

Jamie P. Schnapp

Table of Contents

	Page
Abstract.....	v
Acknowledgments.....	vi
Table of Contents.....	vii
List of Figures.....	ix
1. Introduction.....	1
1.1. Background.....	1
1.2. Related Work.....	4
1.3. Problem Statement.....	6
1.4. Scope.....	7
1.5. Preview.....	7
2. Background.....	9
2.1. Chapter Overview.....	9
2.2. Fabrication.....	9
2.3. Flexure-Beam Micromirror.....	12
2.4. Analytical Model.....	14
2.5. Beam Theory.....	17
2.6. Squeeze-Film Damping.....	21
2.7. Stability.....	23
2.8. Kalman Filter.....	26
2.9. Extended Kalman Filter.....	28
2.10. Linear-Quadratic-Gaussian (LQG) Control.....	29

3. Modeling	31
3.1. Chapter Overview.....	31
3.2. Pull-In Voltage	31
3.3. Effective Spring Constant.....	34
3.4. Parasitic Capacitance.....	37
3.5. Fluid Damping.....	42
3.6. Transient Analysis.....	43
4. State Estimator and Controller Design	45
4.1. Chapter Overview.....	45
4.2. State Estimator Design	45
4.3. Controller Design	52
4.4. Script Implementation	56
5. Results and Conclusions	59
5.1. Introduction	59
5.2. Observer Results.....	59
5.3. Controller Results.....	64
5.4. Conclusions	67
5.5. Future Work.....	68

List of Figures

Figure	Page
1. Packaged scanning micromirrors	1
2. Flexure-beam micromirror device	3
3. PolyMUMPS process layers	10
4. FBMD layout	12
5. FBMD modeled mechanically and electrostatically	14
6. Bifurcation diagram	25
7. Block diagram of closed-loop feedback of the KF	27
8. Three-dimensional model of the FBMD	31
9. Deflection and total charge versus input voltage in CoventorWare	33
10. Simulated mechanical restoring force versus deflection	34
11. Simulated post-process capacitance	38
12. Damping force and deflection versus time	41
13. Mirror plate deflection versus time in COMSOL	43
14. Norton Equivalent Circuit	46
15. Assumed Certainty Equivalence Block Diagram	55
16. Observer-estimated voltage across FBMD and deflection versus time	58
17. Residuals and filter-calculated uncertainty	59
18. Observer error in voltage and in deflection	59
19. KF estimate of voltage across FBMD for diverging deflection	60

20. KF-calculated residuals and uncertainty for diverging deflection	61
21. Observer error in voltage and in deflection for diverging deflection	61
22. Controlled voltage and deflection versus time for y_d of 1 micron	62
23. Residuals and filter-computed uncertainty for y_d of 1 micron	63
24. Controlled voltage and deflection versus time for y_d of 1.5 micron	64
25. Residuals and filter-computed uncertainty for y_d of 1.5 micron	65

LINEAR-QUADRATIC CONTROL OF A MEMS MICROMIRROR USING KALMAN FILTERING

1. Introduction

1.1. Background

In the past decade, the field of MicroElectroMechanical Systems (MEMS) has enjoyed rapidly accelerating scientific research and commercial adoption [63]. Advancements in fabrication techniques and simulation tools have enabled greater system refinement and understanding. As an illustration of the maturity of the field, MEMS-based accelerometers, such as Analog Devices's ADXL-50, have been universally adopted since 2001 for airbag deployment [63], while MEMS pressure sensors are now standard features in automobiles [63], and chips containing millions of MEMS micromirrors, with mean times between failure on the order of 20 years and a trillion cycles, are commercially available [1]. Single micromirrors with two-dimensional scanning capability, as those shown in Figure 1, are commercially available “off-the-

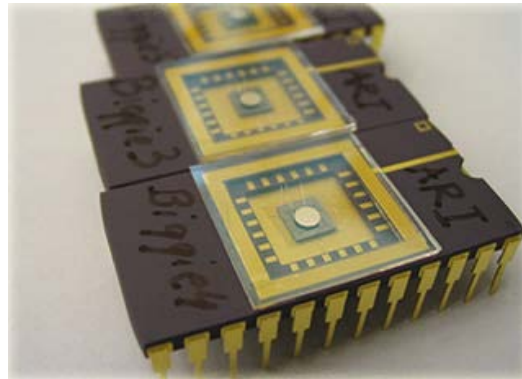


Figure 1: Packaged scanning micromirrors, commercially available from Adriatic Research,

shelf” in standard dual inline packages.

Fabrication variability and analytical complexity, however, continue to limit the growth of MEMS. For the PolyMUMPs process in particular (albeit a pathological example primarily used for education), parameter deviation of 20% from nominal values published by MEMSCAP has been reported [5], all but eliminating the possibility of highly accurate modeling. Exacerbating this problem, variation in device dimensions can be magnified in system-level parameters quadratically or even cubically, depending on application. Consider, for example, a rectangular flexure beam of the classical comb resonator; a 20% decrease in width of this beam will result in a 50% smaller moment of inertia, which will be directly reflected in the effective spring constant of the beam, and thus the resonant frequency of the device. Combine this magnification with complex geometries and strong coupling between the applicable physics regimes, and traditional approaches to actuator design and control become nearly intractable.

The Kalman Filter (KF) is uniquely suited to estimating parameters and operating variables that are otherwise difficult to measure. More commonly used in autopilot and inertial measurement systems, KFs exploit knowledge about system and sensor dynamics, noise sources, and initial conditions to provide a running, quantitative characterization of a system. In this capacity, KFs act as a class of stochastic observers, which can then be used to extend the capability of a controller by increasing the observability of that which is to be controlled. With accurate estimates of physical parameters, the observer increases the controller’s insight into the system, generally allowing more efficient control actions.

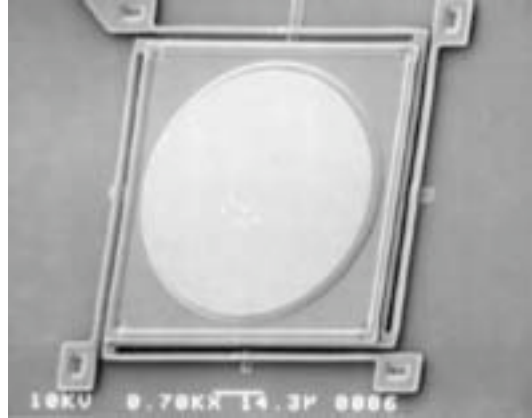


Figure 2: Flexure-beam micromirror device [11]

The flexure-beam micromirror device (FBMD), shown in Figure 2, exemplifies the type of nonlinear, highly dynamic system for which a KF may be employed to great benefit. A well-known artifact of most electromechanical microactuators is the so-called pull-in voltage; that is, the voltage at which mechanical restoring forces cease to balance Coulombic attractive forces, and the electrodes snap together as a result of the lost equilibrium. This condition uniformly occurs at approximately one-third of the total available travel distance, commonly referred to as the “gap,” leaving two-thirds without a stable operating point. Furthermore, such an uncontrolled impact accelerates contact wear and causes hysteresis in the gap versus applied voltage, since stiction (a Van der Waals force that causes two surfaces in contact to be “sticky”) adds to the force needed to return to equilibrium. In the worst case, this stiction is permanent and leads to device failure, which constitutes the major factor in determining device reliability.

Only for testing purposes, however, are FBMDs constructed such that the gap is directly measurable. This is usually accomplished by back-etching through the bottom electrode of the FBMD, shining a laser on the moving plate, and collecting interferometric data, thereby optically measuring the distance travelled by the

micromirror [5]. Another method of collecting the same data without the back-etch is a down-looking interferometer, such as the popular Zygo white-light interferometer; placing a control sensor in the path of incoming signal, however, would inevitably decrease the utility of the micromirror. Furthermore, interferometry takes time to acquire data and signal processing to convert data into a meaningful measurement of displacement, which severely handicaps the bandwidth of any controller implementation. The additional fabrication processing steps, additional light source, and associated electronics needed to perform this measurement, moreover, add system complexity so as to be inappropriate for an array implementation, as well as cost prohibitive for implementation on any commercial scale. The work presented here attempts to demonstrate the utility of using a KF to estimate this gap purely as a function of input current and measured voltage across the FBMD, using known system dynamics, initial conditions, and approximate sensor noise strengths, enabling nearly instantaneous measurement.

1.2. Related Work

Much work has been done to control electrostatic MEMS actuators, most of which with the goals of extending the operating travel range, and/or increasing positioning accuracy [5]. These efforts can be divided into several categories: 1) geometrical, in which the device structure is adjusted to increase the effective mechanical spring constant, or increase the stroke length; 2) open-loop control, which manipulates the input signal to create desired effects based on empirically or analytically identified system parameters; and 3) closed-loop control, which uses some sort of error signal to

tune the input signal. With respect to an intended application, each method has advantages and disadvantages.

Changing the geometry of the device often complicates the fabrication process, with the benefit of relatively simple operation. This is usually done to enhance the effective spring constant, or create and/or control a nonlinear restoring force, thereby extending the actuator stroke. Common themes include a phased flexure [6][33], such that supports and/or beams are activated as deflection increases, effecting a nonlinearly increasing spring constant with increasing deflection; bottom electrode sizing and positioning [11][14], in which the capacitance area or fulcrum position is varied such that increasing deflection exposes more (or less) of the bottom electrode; and optimization of the device structure with respect to the pull-in voltage [18].

Open-loop control attempts to maintain an unstable position by varying the input waveform, despite not knowing the real-time actuator deflection. This variation is based upon insight into the system dynamics, usually from analytical modeling, or empirical system identification. Waveforms may take the form of pulsed voltage [13][29][35], or charge [7][28], or of continuous, “preshaped” signals [12]. While the structure itself remains relatively simple in terms of fabrication, open-loop control requires drive electronics complex enough to generate non-trivial waveforms, and, more importantly, generally features less accurate deflections than similar closed-loop methods as a result of a lack of robustness to process variations, environmental challenges, or deviations from system concept of operations. Inaccurate deflection control does not prevent snap-in, but rather modestly extend the deflection range.

Comprising the majority of research in the area is that of closed-loop control. Efforts range from applying classical linear controllers to simplified equations of motion [3][4][5][10][16][22][25][27][31][32][34][43], to adding compensators to effect feedback linearization [8][17][21][22][28][37][38][39][40][41], to generating fully nonlinear control laws [20][45][46][47][48][49]. Some designs employ full- or reduced-order observers [2][9][15][19][23][25][26][30][32][42][46], which estimate, in real-time, the position and/or velocity of the actuator based upon measured parameters (e.g., capacitance). These observers then update the assumptions made by the controller, making it adaptive. Less common methods include neural networks [1], fuzzy logic [18][19], sliding mode control [36], port-controlled Hamiltonian systems [22], and passivity-based control [23][24][26].

1.3. Problem Statement

The instability of electrostatic flexure-beam actuators beyond one-third of the gap across which the potential is applied leads to a nonlinear “snap-in” effect that limits the effective range of controllable actuation and dramatically reduces operational lifetime. From a control design standpoint, this problem is exacerbated by limited system observability (nominal structures exclude feedback sensors) and wide parameter variability. The Kalman Filter, used in conjunction with a Linear-Quadratic-Gaussian (LQG) controller, is uniquely suited to estimate unobservable states in the presence of such parameter variability and noise sources, owing to its simple measurement system, scalability to large arrays, and straightforward digital implementation. This powerful

combination enables real-world, full-gap actuator positioning and controllable snap-in, thereby eliminating the dominant failure mechanism.

1.4. Scope

This work is limited to a proof-of-concept observer/controller pair as applied to a single micromirror geometry. While the approach presented is equally valid for alternative geometries, material systems, and actuator schemes, only one will be explored. Furthermore, no attempt to create a deployable system will be made. Issues to be considered for robustness enhancement, such as external shock or vibration forces, changes in ambient temperature or pressure, and performance degradation over time, will be left to follow-on research. Lastly, since this work is a proof-of-concept, hardware implementation will be simulated and limited to that which is required for developmental validation of the control algorithms; electronics integration, footprint minimization, and packaging will also be left for future work.

1.5. Preview

This research is presented in five chapters. Chapter 1 introduces the problem, motivates the solution, and delineates past research with similar aims. The problem statement clearly identifies the goal of the work, while the scope sets boundaries and specifies starting assumptions.

Chapter 2 presents background theory in sufficient detail such that the reader can understand the design process described in later chapters. In particular, a summary is

included of PolyMUMPs fabrication steps, the mechanical and electrostatic physics of flexure-beam actuators, and Kalman Filter and LQG controller operation.

Chapter 3 describes the modeling and the control law development. The COMSOL Multiphysics modeling and simulation software is used to generate nominal charge and position versus time trajectories, upon which the KF is based. Lastly, the LQG controller is derived from actuator position and velocity requirements.

Chapter 4 discusses the performance of the control laws developed in Chapter 3. Results from MATLAB simulations are compared to the nominal trajectories by statistical analysis, with the system performance indicated by the state error means and covariances. A micromirror fabricated in PolyMUMPs is then used to accomplish a hardware-in-the-loop test for real-world performance, the latter characterized by comparing discrete gap measurements to the KF estimate.

Chapter 5 provides conclusions and suggestions for future work. The system is judged based upon the results in Chapter 4, and performance shortfalls highlighted and explained.

2. Background

2.1. Chapter Overview

The purpose of this chapter is to summarize the foundations upon which this work is built. First, the PolyMUMPs fabrication process is described step by step, and key artifacts highlighted. Second, the FBMD layout is presented in the context of PolyMUMPs fabrication. Third, a first-order analytical model is derived from the respective physical regimes (mechanical, electrostatic, and fluid dynamics). After this derivation, the stability of the model is analyzed for controller suitability. Last, the Kalman Filter and Linear Quadratic Gaussian control are introduced for further discussion in Chapter 4.

2.2. Fabrication

The MEMSCAP Multi-User MEMS Processes (MUMPs) is employed to fabricate prototype MEMS devices for government, industry, and academia worldwide. In particular, PolyMUMPs features three, surface-micromachined polysilicon layers, two of which are releasable (that is, the layer immediately beneath can be etched away to “release” the polysilicon above it), and one metallization layer. The fabrication process is fixed and enforced by design rules specified by MEMSCAP [66]. These are described below and illustrated in Figure 3 in order to elucidate eccentricities of the process.

First, n-type (100) silicon wafers, 150 millimeters in diameter, are pre-treated by heavily doping the surface with phosphorus in order to help prevent charge accumulation between the substrate and isolation layers. This isolation layer is then created by 0.6 μm

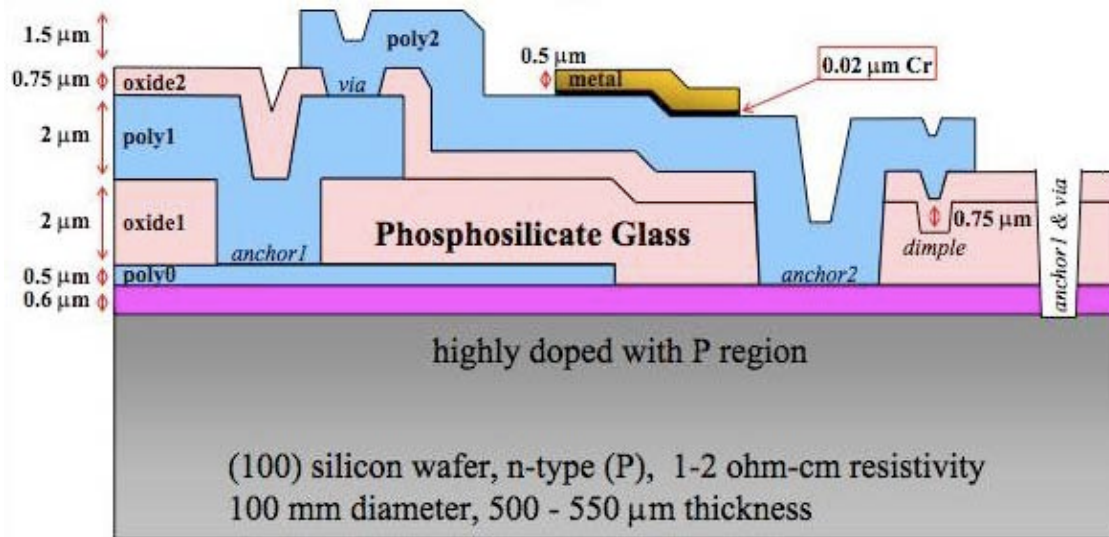


Figure 3: PolyMUMPs process layers [66]

of low-stress low-pressure chemical vapor deposition (LPCVD) silicon nitride, followed by a $0.5 \mu\text{m}$ polysilicon layer, called *poly0*. This polysilicon layer is also deposited by LPCVD, photolithographically patterned, and etched via plasma etching. The first sacrificial layer, *oxide1*, consisting of $2.0 \mu\text{m}$ of phosphosilicate glass (PSG) [66], is deposited next by LPCVD at $580 \text{ }^\circ\text{C}$ and then annealed at $1050 \text{ }^\circ\text{C}$ in argon. This anneal reduces residual stress and dopes the lower polysilicon layer to a concentration of $1 \times 10^{19} \text{ cm}^{-3}$ [67]. Stiction-preventing dimples are created by reactive-ion-etching (RIE) $0.75 \mu\text{m}$ holes into the PSG layer at this stage. Anchor points, which connect the second polysilicon layer and the substrate (*anchor1*), are similarly produced by RIE immediately following the dimple etch.

Starting with the deposition of the polysilicon layer, the process is essentially repeated, with some differences. The second polysilicon layer, *poly1*, is $2.0 \mu\text{m}$ thick and deposited by LPCVD at this step. This is followed by a PSG layer to act as a hard mask

for the polysilicon etch, which is subsequently removed by RIE. Next, yet another PSG layer is deposited $0.75\ \mu\text{m}$ thick and annealed to act as the second sacrificial oxide layer, *oxide2*. Two different etch masks are used at this point: the first to create a connection between the second and third polysilicon layers (*poly1-poly2 via*); and the second to connect either the first and third polysilicon layers, or *poly2* to the nitride layer (*anchor2*).

The last polysilicon layer, *poly2*, is now deposited $1.5\ \mu\text{m}$ thick. A $0.2\ \mu\text{m}$ PSG layer is again used as a hard mask and dopant source for the third polysilicon layer; each are patterned, and the PSG removed as before. The final layer, *metal* ($0.5\ \mu\text{m}$ of gold with a thin chromium adhesion layer), is lithographically patterned, deposited by electron beam evaporation, and patterned using lift-off. With the fabrication complete, the wafers are diced, sorted, and shipped.

Three points must be emphasized. First, the process inherently produces conformal layers; that is to say, if a design contains a feature in *poly0*, the poly layers above it will drape over the *poly0* shape, like a rug lying over a book. The effect is that the flexure-beam actuators fabricated in PolyMUMPs are not the straight beams commonly modeled by Newton-Euler analytical beam-bending equations. They instead have angles, which will affect the restoring force generated by the beam for a given load. Second, successive layers of polysilicon undergo fewer anneal stages, which affects both the conductivity and the strength of the layer. In particular, the Young's Modulus of the first polysilicon layer has been measured to be approximately 20% less than the second, while exhibiting half the resistivity [68]. Third, residual stress must be managed

thoughtfully in PolyMUMPS devices. As an artifact of bonding two materials with different coefficients of thermal expansion, residual stress manifests most apparently as bowing in layers of *poly2* and *metal*. A bowed flexure beam will deflect differently than an unbowed beam of similar composition, while a bowed mirror will feature a different capacitance due to the non-uniform gap. These effects will be studied in Chapter 3.

2.3. Flexure-Beam Micromirror

The micromirror design on which the present work is composed is shown in Figure 4, as fabricated in PolyMUMPs, described above. The mirror plate is a $100\ \mu\text{m}$ by $100\ \mu\text{m}$ *poly1* square, with five etch holes to ensure all oxide is removed with the

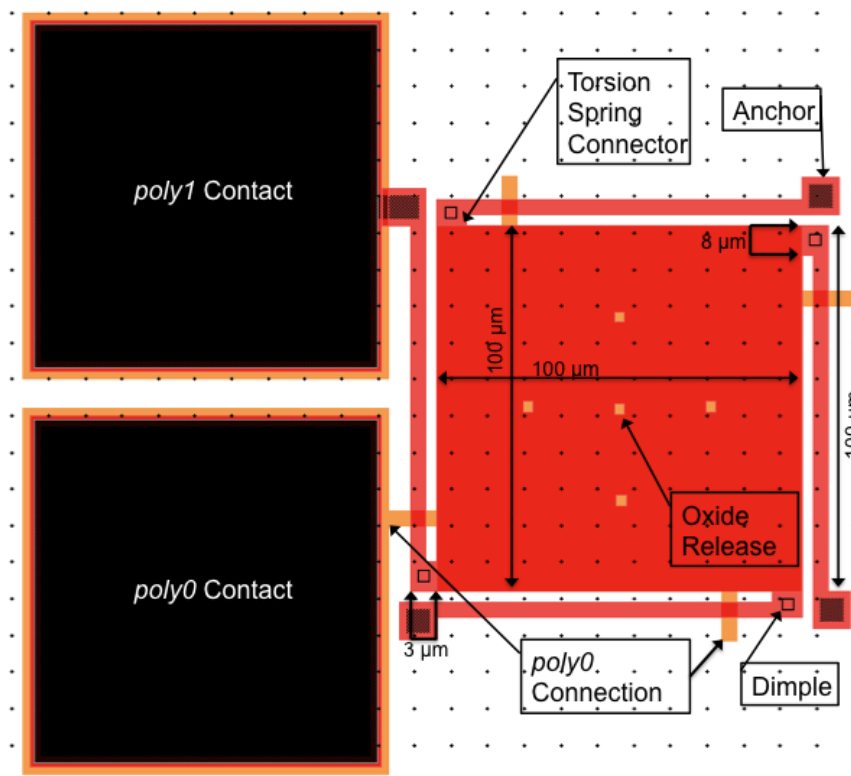


Figure 4: FBMD layout

release process (shown as orange in Figure 4), each $3\ \mu\text{m}$ by $3\ \mu\text{m}$. A *poly0* square of dimensions equal to the *poly1* mirror plate is immediately below the plate (orange in the figure) and serves as the bottom electrode, typically held at ground. Note that the *poly0* connection between the bonding pad and the electrode is reflected on each side of the square; this is to ensure symmetry in the three-dimensional shape of the flexures given the conformal process. That is to say, the released flexure beam will have upward and downward bends with respect to the plane of the substrate, as it conforms over the *poly0* connection. The symmetry of the electrode encourages uniform response from each of the four flexure beams. The flexures are each $100\ \mu\text{m}$ long by $3\ \mu\text{m}$ wide *poly1* beams, attached to the mirror plate by $3\ \mu\text{m}$ long by $8\ \mu\text{m}$ wide *poly1* connectors. These connectors in this application act as torsion springs, as the faces attached to the mirror and flexure beam rotate with respect to each other as the mirror deflects. Located on the substrate side of each of these connectors is a dimple, which prevents the mirror plate from coming into physical contact with the bottom electrode, minimizing the possibility of stiction, and electrical shorting. $10\ \mu\text{m}$ by $10\ \mu\text{m}$ *poly1* anchors attach each of these beams to the substrate, thereby fixing one end to a rigid post (the other end is only fixed to the torsion spring connector, and is allowed to move in space). One anchor point is attached to a $50\ \mu\text{m}$ by $50\ \mu\text{m}$ *poly2* bond pad, which creates a conductive path between the mirror plate and the bond pad and enables an external voltage source to generate a potential difference between the plate and bottom electrode.

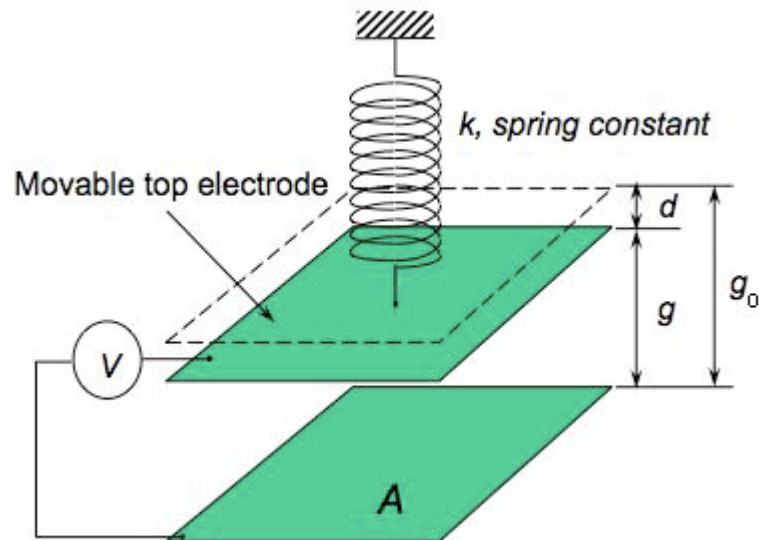


Figure 5: FBMD modeled mechanically as a simple harmonic oscillator and electrostatically as a parallel plate capacitor

2.4. Analytical Model

Analytically modeling the FBMD promotes understanding of the pull-in phenomenon and allows meaningful exploration of possible solutions. As mentioned above, the FBMD is held in equilibrium by two opposing forces: the mirror plate is electrostatically attracted down towards the bottom electrode as a result of an applied potential; and the flexure beams mechanically resist the electrostatic force and restore the plate to an initial, quiescent distance, g_0 , away from the bottom electrode, as illustrated in Figure 5. The output restoring force of the flexures is generally modeled, to first order, by Hooke's Law, i.e., linearly proportional to the amount of induced deflection in the beams, with the proportionality constant thought of and referred to as the spring constant, k :

$$F_m = kd = k(g_0 - g) \quad (1)$$

where g_0 is the quiescent gap distance; d is the mirror plate deflection distance from g_0 ; and g is the gap distance. Various schemes are used to adjust the effective mechanical restoring force in order to meet system design requirements for resonance frequency, operating voltage, and the gap-versus-voltage hysteresis. These schemes include changing the beam material or geometry (e.g., I-beam-like cross section); increasing the number of flexures or attachment point (e.g., attaching at the middle of the mirror edge rather than the corner shortens the beam and increases k , as shown in Section 2.5.3); and lever arm implementation [14]. A Duffing spring model may increase accuracy by adding a cubic deflection term fitted to data by proportionality constant. This model is one method to account for nonlinear spring softening with increasing deflection. The literature reports yet more complicated effects [11].

By contrast, the electrostatic force is inversely proportional to the square of the distance between the mirror plate and the bottom electrode plate, g , and proportional to the square of the potential difference across the plates. This force is derived from the well-known expression for the energy U stored in a parallel-plate capacitor in steady-state and the definition of capacitance:

$$U = \frac{Q^2}{2C} = \frac{1}{2}CV^2 = \frac{1}{2} \frac{\epsilon_0 A}{g} V^2 \quad (2)$$

where Q is the total charge on the two plates; C is the capacitance; V is the potential difference across the plates; g is the distance between the mirror plate and the bottom electrode as above; A is the area of the plate; and ϵ_0 is the free space permittivity. The

force is then defined as the negative gradient of the potential energy. Since this system has only one degree of freedom, the gradient is simply the first partial derivative with respect to g :

$$F_e = -\frac{\partial U}{\partial g} = \frac{1}{2} \frac{\epsilon_0 A}{g^2} V^2 \quad (3)$$

Although Equation (3) increases the polynomial order of the static equation, as well as numerical complexity as a result of the discontinuity at zero gap, it is far from a complete characterization of reality. First, each of the four flexures accumulates charge, thereby acting as four additional capacitors with respect to the ground plate and varying with deflection. Second, the parallel plate model assumes parallel, infinite plates. Since the FBMD is finite, the electric field is not wholly contained between the plates, but rather extends outside, giving rise to what are known as fringing fields. Moreover, the parallel plate model neglects the thickness of the plate; in reality, the sides of the plate also generate electric fields, which must be accounted in the aggregate electrical potential energy. Last, the parallel plate model assumes a uniform gap, but as mentioned in Section 2.2, the mirror plate is not perfectly rigid and may demonstrate some measure of bowing in the center. Although to lesser effect, the flexure beams may also demonstrate bowing in addition to the bump discussed in Section 2.2 and shown in Figure 8, either down as a result of the weight of the mirror plate, or up as a result of residual stress. The capacitance of the FBMD is simulated in Chapter 3, and the magnitude of these non-ideal extensions will be quantified to show that the fringing fields are by far the largest non-ideal effect; flexure capacitance and plate thickness contributions are negligible.

2.5. Beam Theory

2.5.1. Introduction

Beam deflection is described analytically by the Euler-Bernoulli equation for beam bending. As a differential equation, any of uniform or point loads and moments can be used as forcing functions, and fixed (clamped), free, or simply supported end faces may be used as boundary conditions. The equation is a simplification of linear elasticity theory with the following assumptions: the beam is subject only to pure bending, i.e., no torsional or axial loads; the material is isotropic and homogeneous, i.e., the flexural rigidity is constant; the material is linearly elastic and will not reach the plastic deformation limit, i.e., Hooke's Law is obeyed; the beam is initially straight with constant cross-section throughout; an axis of symmetry is in the plane of bending; the proportions of the beam are such that it would fail first and foremost by bending; and cross-sections of the beam remain planar during bending. Ineluctable deviations from these assumptions are addressed after the derivation.

2.5.2. Derivation

The static Euler-Bernoulli beam equation may be shown to be the result of combining four basic relationships. First, a kinematics equation specifies how the beam moves. In one-dimensional, linear beam theory, this amounts to describing how each point in a lengthwise cross-section of the beam is displaced with deflection; this displacement is equivalent to the strain in the beam. By assuming that deflections are small and that the neutral plane does not change in length under load, the beam bends into an arc of curvature χ , and the angle θ through which the widthwise cross-section

moves can be equated using the small angle approximation to the negative of the slope of the deflection w :

$$\text{---} \quad (4)$$

Second, a constitutive equation relating how the beam moves in response to external forces is specified. For approximately linear materials, Hooke's Law is employed:

$$(5)$$

where σ is stress, ε is strain, and E is Young's Modulus. Third, using so-called force resultant equations, the point-by-point aggregate effect of these external forces in a widthwise cross-section is quantified by integrating the appropriate stress over the cross-section and equating the result to moments M and shear forces V :

$$(6)$$

Last, equilibrium is established for each infinitesimal length by equating the change in shear force to pressure load p and the change in moment to the shear force resultant:

$$\text{---} \quad (7)$$

$$\text{---} \quad (8)$$

Using algebra, the ratio of pressure load (force per unit length) to rigidity can be shown to equal the fourth derivative of deflection with respect to length, i.e., the canonical Euler-Bernoulli beam bending equation:

Each successive derivative of the deflection given by the Euler-Bernoulli equation has a corresponding physical interpretation. The first derivative with respect to the length along which the beam deflects is, for small values, the angle between the neutral axis and the beam. The second derivative is the net moment on the beam, while the third derivative is the net shear force. Net load per unit length is represented by the fourth derivative. Each of these may balance a static or dynamic forcing term that models the type of operation the beam is performing; e.g., a diving board would have a point load (force multiplied by a Dirac delta function with domain shift corresponding to the position of the force) as a forcing term for the fourth derivative. As stated above, several support types can be represented through the appropriate use of boundary conditions. For example, setting the deflection and slope of one end to zero models a fixed support at that end, while no deflection and no net moment represents a pin connection. Boundary conditions must be set carefully in order to properly capture the physics.

2.5.3. Lumped-model Effective Spring Constant

A lumped-model parameter consolidates the gamut of complex physical processes into a “black box,” a computationally simple—or at least more straightforward—abstraction that approximates an output for a given input. This abstraction often imitates the functional form of a more familiar relationship, e.g., a mass-spring system or basic circuit. In the present case, the deflection of a flexure beam in an FBMD is modeled as a simple, linear spring obeying Hooke’s Law, with a restorative force linearly proportional

to the distance deflected. The process begins with the Euler-Bernoulli equation for beam supporting a point load at the free end, with the latter realized in boundary conditions. In particular, the fourth derivative of deflection with respect to beam length, i.e., pressure per unit length, is set to zero. Assuming a constant flexural rigidity EI , both sides of this equation are integrated four times, yielding a cubic polynomial for deflection versus length position with four indeterminate constants of integration. Boundary conditions are then applied: position and slope of the fixed end of the beam are set to zero; the slope of the free end is set to zero as a result of being attached through a hinge to the mirror plate; and the shear force at the free end of the beam is set to equal the point load. After solving for the deflection at the free end, the point load is solved for as the dependent variable in terms of this deflection; the result is an equation that emulates Hooke's Law for linear springs:

$$\text{---} \quad \text{---} \quad \text{---} \quad (10)$$

The proportionality constant, twelve times ratio of the beam flexural rigidity and the length cubed, is considered as the effective spring constant, "lumped" into which are the essential physics quantified by the Euler-Bernoulli equation. As each of the four flexures contributes this restoring force, the total mechanical restoring force is provided by four springs, thus the effective spring constant is multiplied by four.

2.5.4. Non-idealities / Extensions

The above litany of constraining assumptions can, in several cases, be modified to extend the validity of the equation. First, beam dynamics may be analyzed by the

addition of the second derivative of deflection with respect to time, scaled by mass per unit length of the beam, to the left-hand side of Equation (9). Second, superposition may be employed to model three-dimensional, distributed, transverse loading, as well as composite beams through the flexural rigidity term. Materials not obeying Hooke's Law may be modeled by the appropriate constitutive equation describing the relationship between stress and strain of the material system. In this way, viscoelastic or plastic deformations and nonlinear material behavior are incorporated, thereby generalizing the Euler-Bernoulli equation. Geometrically nonlinear beams may be accounted for by dividing the second derivative of deflection by the three-halves power of the slope squared with unity offset. This divisor enables a more accurate description of an initially curved beam, e.g., a cantilever with residual stress, as physically motivated in Section 2.2. Large deflections (i.e., bending radius equal to or smaller than one-tenth of the cross-section) may be approximated by multiplying the moment of inertia by a function that increases inversely with the radius of curvature, and by adding another moment term to the second derivative of deflection that does the same. Last, thick beams, for which the transverse shear strain is non-negligible, must depart from Euler-Bernoulli treatment entirely and be analyzed with the Timoshenko beam theory.

2.6. Squeeze-Film Damping

To guarantee a thorough analysis, the application of MEMS devices outside a vacuum should take into account the effects of submersion in a viscous fluid. For the dynamic operation of the FBMD used in the present work, air between the bottom electrode and mirror plate is forced outward as the mirror is pulled down, while it is

conversely pulled inward as the mirror is restored to its initial position. This movement of air dissipates energy in the system by opposing the motion of the mirror in both directions. As such, it can be modeled as a dashpot on its effect in a mass-spring system.

A number of simplifying assumptions can make tractable the Navier-Stokes equation—a nonlinear partial differential equation governing fluid dynamics. First, the fluid is assumed to be isothermal and Newtonian; that is, the ratio of the shear stress exerted by the fluid (drag) to the rate of strain is equal to the viscosity of the fluid, a constant. Ignoring thermal variation is equivalent to assuming uniform proportionality between density and pressure. Second, viscous forces (the fluid's resistance to deformation by shear or tensile stress) are assumed to dominate over inertial forces (the fluid's resistance to changes in momentum), known as Stokes flow, or creeping flow; this is due to the dimensions of the FBMD being small enough that the dynamic viscosity of air is much larger than the mass of the air in the cavity. As a result, the general Navier-Stokes equation can be simplified to the Reynolds equation, another second-order partial differential equation closely resembling the classical heat equation with internal heat generation [63]. Further, assuming a uniform fluid thickness, small pressure variation with respect to the ambient, and small mirror plate displacements reduces the Reynolds equation to a simple Poisson's equation, readily solved analytically using a Green's function. The result is in a form germane to the present work, namely, a function that is linearly proportional to the velocity of the mirror plate to within a constant.

A more exact formulation takes into account unique features of the MEMS, such as compressibility effects, slip-conditions, and large mirror plate displacements.

Compressibility effects describe the disproportionate fluid outflow as a result of mirror displacement and can be treated as additional stiffness in the mass-spring system [51]. Slip-conditions reduce the damping constant by taking into account the lack of continuum as the mean free path of fluid molecules becomes significant with respect to the fluid thickness [56]. The solution to the Poisson's equation displays a strong dependence on film thickness, so it is intuitive to understand that, as the mirror plate displacement increases with respect to the nominal, the damping coefficient will increase as well [69]. All three of these effects can be taken into account to first order by multiplying by appropriate scaling factors.

2.7. Stability

To maintain equilibrium, the electrical and mechanical forces must be equal. By Equation (3), the electrical force increases quadratically with the beam deflection, while the mechanical restoring force increases linearly. The voltage corresponding to the largest stable deflection, known as the pull-in voltage, can be found by equating the mechanical (Equation (1)) and electrical (Equation (3)) forces, solving for the voltage, and finding the minimum voltage with respect to the distance between the plate and the bottom electrode, resulting in the following:

$$\frac{1}{2}k_{eff}x^2 = \frac{1}{2}\epsilon_0\frac{V^2}{d^2}x^2 \quad (11)$$

where k_{eff} is the total effective spring constant for all flexure beams.

The steady-state stability of the canonical FBMD is most often characterized in terms of the pull-in point. Going a step further, however, it can be shown (by equating

Equations (1) and (3) and solving for g) that, for simple models at a particular voltage, exactly two steady-state equilibrium solutions exist: one globally stable position in the gap and one unstable position. The latter corresponds to a deflection past one-third of the total gap. At the pull-in point, one solution exists, beyond which all positions become unstable. Physically, this phenomenon is a result of the inability of the linear mechanical spring to maintain equilibrium with the quadratic electrostatic force throughout the gap; as the input voltage or charge increases, causing increased beam deflection and decreased electrode separation, both the electrical attractive force and mechanical restoring forces increase. From zero deflection to the pull-in point, the mechanical force increases enough to maintain steady-state equilibrium with the electrical force, but after this point, the mechanical force can no longer increase by a large enough amount to balance the electrical force with its greater rate of increase. Having lost equilibrium, the top electrode snaps into the bottom electrode with an acceleration proportional to the net force, resulting in the eponymous phenomenon.

By including the dynamics of the system, analytical characterization of the pull-in phenomenon can be obtained. Inertial and damping forces are added to the steady-state equation as in the following:

$$\text{---} \quad (12)$$

where A , B , m , k , ϵ_0 , and V are the mirror plate area, damping coefficient, plate mass, effective spring constant, free-space permittivity, and applied voltage, respectively. The

variables of Equation (12) are then made nondimensional for ease of analysis through the following translations:

$$\begin{aligned} & \text{---} \\ & \text{---} \\ & \text{---} \\ & \text{---} \end{aligned} \quad (13)$$

where t is time, to produce

$$\text{---} \quad \text{---} \quad (14)$$

A bifurcation diagram of the static, non-dimensionalized system is shown in Figure 6. The dotted line corresponds to the fold, i.e., at two-thirds of the quiescent gap space, g_0 , only one ζ (non-dimensionalized input voltage) exists. The shaded gray area corresponds to the unphysical region where the deflection is greater than g_0 . As asserted above, for each voltage input ζ less than unity, two χ values exist: one greater and one less than one-third. It can be shown that the former is an unstable equilibrium and the latter stable [63]. The existence of equilibria, however unstable, beyond a third of the gap motivates the use of closed-loop control.

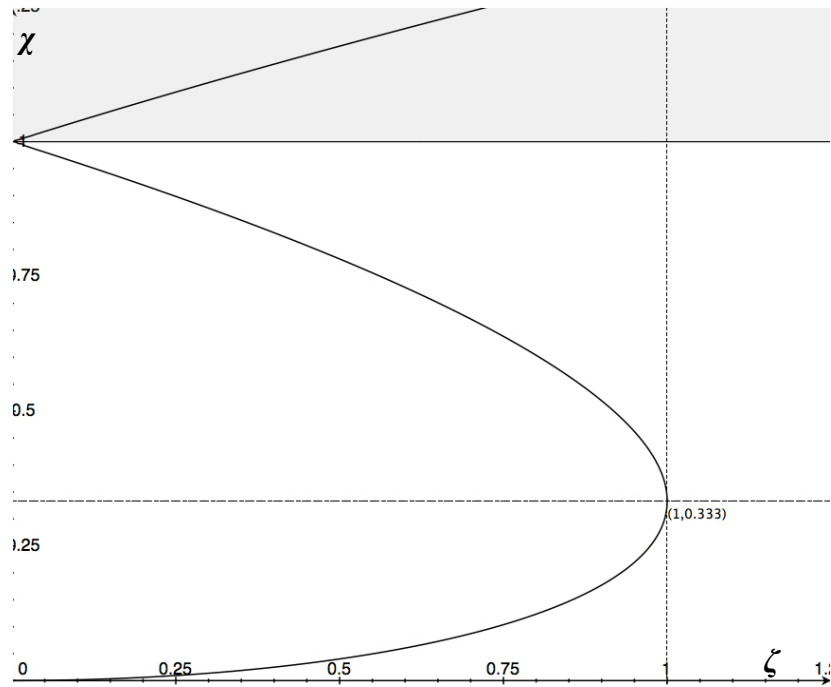


Figure 6: Bifurcation diagram of static, non-dimensional system

2.8. Kalman Filter

A Kalman Filter (KF) incorporates sets of equations describing system dynamics into a state-space model, which it combines with known inputs, initial conditions, and model uncertainties in order to estimate how the states—observable or not—and their associated covariances change over time. In the basic form, this model is a matrix of linear, first-order differential equations, discretized for easy use with digital computers and sample-and-hold sensors. Model uncertainty is assumed to be described by a Gaussian distribution with zero mean; in this way, only the first two statistical moments need monitoring. Deviations from this assumption, such as biases or non-Gaussian processes, can be modeled by augmenting the state dynamics model with noise transfer

functions driven by white Gaussian noise. Estimates of the states' evolution, propagated forward in time using the dynamics model, are refined each sample period by reading a measurement, and calculating the divergence between the actual and expected values for that measurement. This divergence, known as the residual or innovation and shown in Figure 7, provides real-time performance data of the KF; modeling inadequacies will manifest most frequently as spikes, biases, or divergence. The filter gain is then updated based on knowledge of uncertainties in the measurement process and dynamics model by taking the ratio of the dynamics covariance and the residual covariance. The product of the new gain and residual is added to the estimate, generating a state estimate for the next sample period, which serves as the output of the filter. A high filter gain has the effect of weighting the measurement more than the expected value in the KF output, while a low gain has the opposite effect.

The importance of the residual data must be emphasized, as it constitutes the primary means by which the adequacy of the dynamics model may be quantitatively measured. Real-world system deployments do not, in general, enjoy access to truth data at all, much less in real-time; as such, absolute estimation errors with respect to truth may not be quantified. In lieu of truth data, KF designers analyze residual data for indications of model inadequacies. Residual data from an adequate dynamics model will feature a zero mean, no spikes, and root-mean-square values for each measured state equal to or less than system tolerances for deviations. Plots of residual data will be presented in Chapter 5 for the current system and analyzed using these metrics.

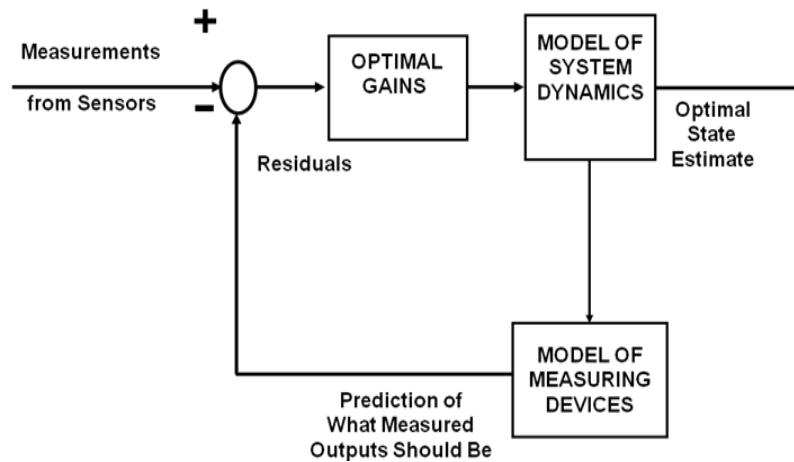


Figure 7: Block diagram illustrating closed loop feedback of the KF

2.9. Extended Kalman Filter

The Extended Kalman Filter (EKF) expands upon the operation of the linear KF by taking into account nonlinearities inherent in the dynamics of the system, without working with the nonlinear equations directly. Using the current state estimate as the operating point, the EKF employs a first-order Taylor polynomial to describe the instantaneous system dynamics, which is then used, along with covariance and measurement data as in the KF, to produce a new state output. A consequence of this is that the matrices required to generate the state estimate are not precomputable as they are for the linear KF, thus increasing computation time considerably.

The advantage of this scheme is greater accuracy in estimating strongly nonlinear effects than a KF with a system dynamics model linearized about a static operating point; significant errors can be the result of neglecting strong nonlinear effects, or poor choice

in operating point. While the penalty of computation is undeniably greater than that of a linear KF, it remains less than the direct use of nonlinear equations, with acceptable accuracy for a variety of applications.

2.10. Linear-Quadratic-Gaussian (LQG) Control

The LQG controller minimizes a quadratic cost function assigned to some or all states of a linear or linearized, stochastic system that is disturbed by additive, white Gaussian noise. Continuous or discrete measurements, functionally related to some or all states, are assumed to be corrupted by additive, white Gaussian noise of zero mean and fed back to the controller. Although assumed to be not applicable here, non-zero-mean noise sources may be modeled by an appropriate shaping filter driven by zero-mean, white Gaussian noise. For the purposes of this work, discrete-time sensor data is assumed to be available as the analog-to-digital conversion of sampled, continuous-time data.

The cost function is defined as the first moment of the sum of the states and control inputs over all time and the desired final state, each squared and weighted according to the constraints of the design and the tractability of the problem. Equivalently, states can be replaced by expressions quantifying deviation from a reference trajectory. In either case, control inputs are found such as to minimize the cost function, with a conceptual “control energy” commensurate with their respective weights. That is to say, the larger the weight, the larger the control effort is expended in driving the state or deviation to zero, or the smaller the control input. The former is useful in accurate trajectory tracking applications, for example, while the latter might conserve

finite available energy or smooth the controller response.

Minimization of the cost function is accomplished by solving a trio of Riccati differential equations, two running forward in time and one running backward. Those running forward model the state and covariance dynamics and constitute the estimator problem, as solved by the KF and EKF described above and shown in Figure 7 as “Optimal State Estimate.” The backward-running equation solves for the feedback gain matrix, the product of which, with the state estimate (i.e., the output of the KF), determines the gains in the general control law to be applied to the system, as well as the “Model of System Dynamics” box in Figure 7. This input is submitted to a zero-order hold and applied at the start of the next sample period. The control law for this work is derived and specified in Chapter 4.

3. Modeling

3.1. Chapter Overview

An accurate model is essential to the function of an observer such as the Kalman Filter. The observer estimates system states—such as velocity or accumulated charge—and disturbances using knowledge from the model and about the passage of time. Typically, as it is here, the model is a state-space representation of the relevant equations of motion.

This chapter is devoted to the development of such a model for the micromirror described in Chapter 2 by means of simulation and analysis. Various nonlinearities particular to the FBMD under consideration were introduced in Chapter 2 and will be quantified here through simulation. First, a pull-in voltage study is performed in CoventorWare, from which parasitic capacitance and effective spring constant are derived. Next, squeeze-film damping is modeled in COMSOL Multiphysics. These effects are combined into a governing equation of motion, which is solved in MATLAB in order to characterize nonlinear transients.

3.2. Pull-In Voltage

CoventorWare contains an algorithm to detect pull-in conditions during its simulation of electromechanically deformed geometries. When engaged, the algorithm checks the calculated displacement for divergence, indicating a pull-in condition. CoventorWare then simulates an input equal to the mean of the last converging and diverging inputs, iterating until either the simulation takes a maximum number of steps,

or the result is less than a set tolerance—that is, a change in calculated deflection. The result of this iteration constitutes the last point of stable equilibrium before pull-in. The pull-in voltage for the present study’s nominal FBMD is calculated in this manner.

A three-dimensional model of the FBMD is created first by drawing its layout in Tanner L-Edit. This layout file specifies, based on user input, the length and width of all desired layers in the PolyMUMPS process. The file may be imported into CoventorWare and, when combined with the appropriate PolyMUMPS fabrication process definition, which specifies the process described in Chapter 2 in a standardized way, CoventorWare creates a three-dimensional model, complete with material definitions and layer thicknesses (Figure 8). Note the conformal nature of the process reflected in the shape of each of the flexures via the rectangular “bump” near the supports.

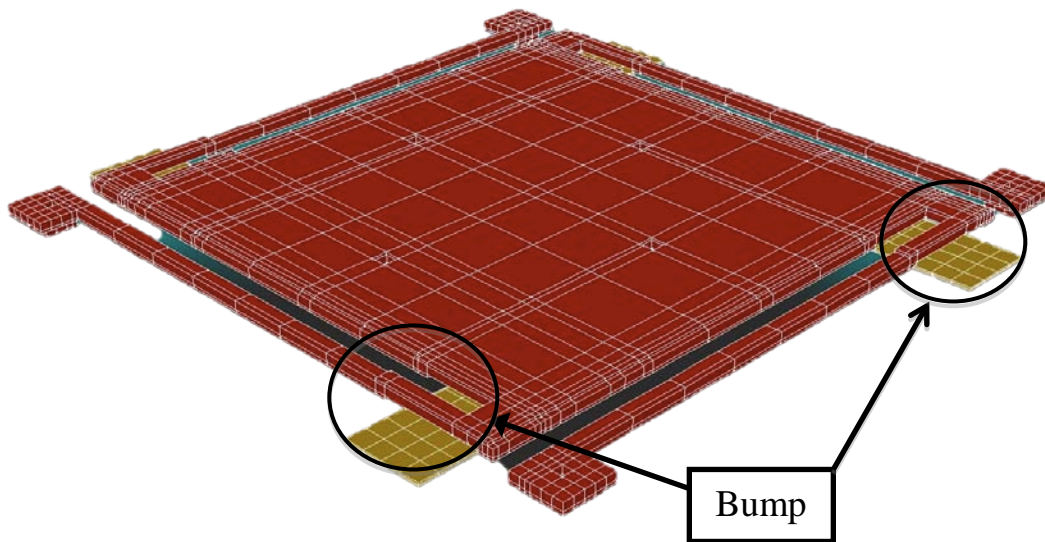


Figure 8: Three-dimensional meshed CoventorWare model of the FBMD with an input voltage of 8 V.

The pull-in study begins by specifying mechanical and electrical boundary conditions: the *poly0* layer is immobile and connected to the electrical ground; the *poly1* flexure supports are immobile; no external mechanical load is applied to the mirror plate or flexures; no mechanical contact between surfaces; and *poly1* is connected to the input voltage. As such, the *poly1* flexures and mirror plate are free to respond to electrical and mechanical forces and move in space. With boundary conditions in place, an input voltage trajectory is set in CoSolveEM to be applied to the FBMD's input—in this case, a voltage ramp from 0 V to 25 V in 0.5 V steps. This voltage range was determined by solving Equation (11) with the FBMD dimensions specified in Chapter 2 and the parameters measured by MUMPS in Run 77 (composite Young's Modulus E of 131 GPa), yielding an analytically expected pull-in voltage of 18.35 V. Equation (11) does not take into account any of the non-idealities described in Chapter 2, so the simulated voltage range was well in excess of the analytical pull-in point to ensure pull-in was captured. Also note that the CoventorWare simulation assumes steady-state conditions.

The simulation is executed, and the pull-in voltage is found to be 21.44 V (Figure 9). For each input voltage in the trajectory up to pull-in, the corresponding mechanical force, electrical force, total charge accumulated in *poly1*, total capacitance, and deflection are calculated. These results show strongly nonlinear mechanical force versus voltage, as well as nonlinear charge versus voltage, indicating a nonlinear parasitic capacitance. Each of these will be discussed in the following sections.

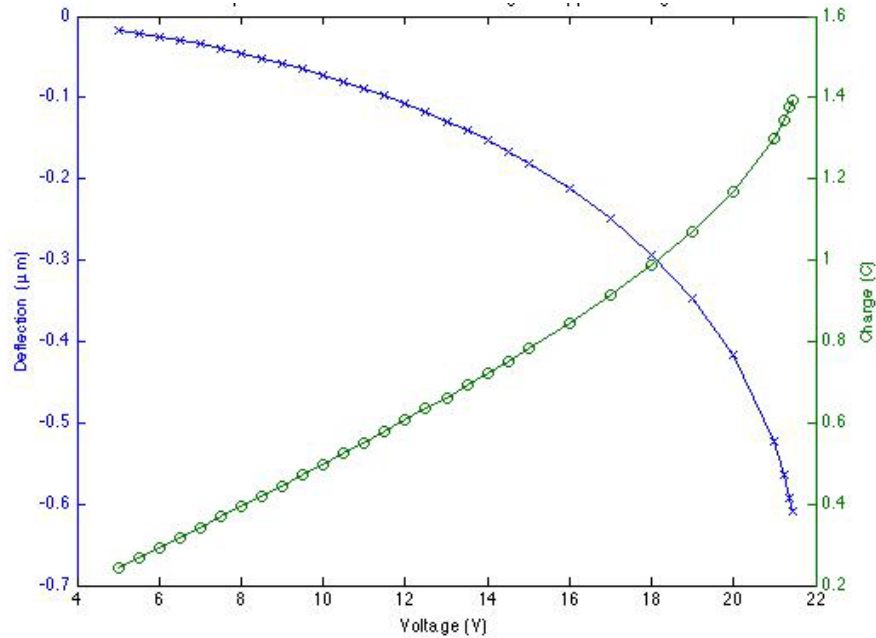


Figure 9: Deflection and Total Charge versus input voltage; pull-in occurs at 21.44 V

3.3. Effective Spring Constant

In Chapter 2, a simple analysis based on Euler-Bernoulli equations for beam bending, shown in Equation (10), was presented to be used as a lumped model parameter in a mass-spring-damper construct. This equation yields a value of 12.576 N/m for an effective linear spring constant using the same Young's Modulus as above of 131 GPa. This analytical value is now compared against a full three-dimensional simulation in CoventorWare, which includes the rigid support stacks, hinges, and residual and internal stresses. To enable a direct comparison, the simulated mechanical force is plotted against geometrical deflection from rest height, on which a linear regression is performed, forcing the zeroth order term to zero (Figure 10). The slope of this line, corresponding to the simulated effective spring constant, is found to be 15.056 N/m, with a correlation

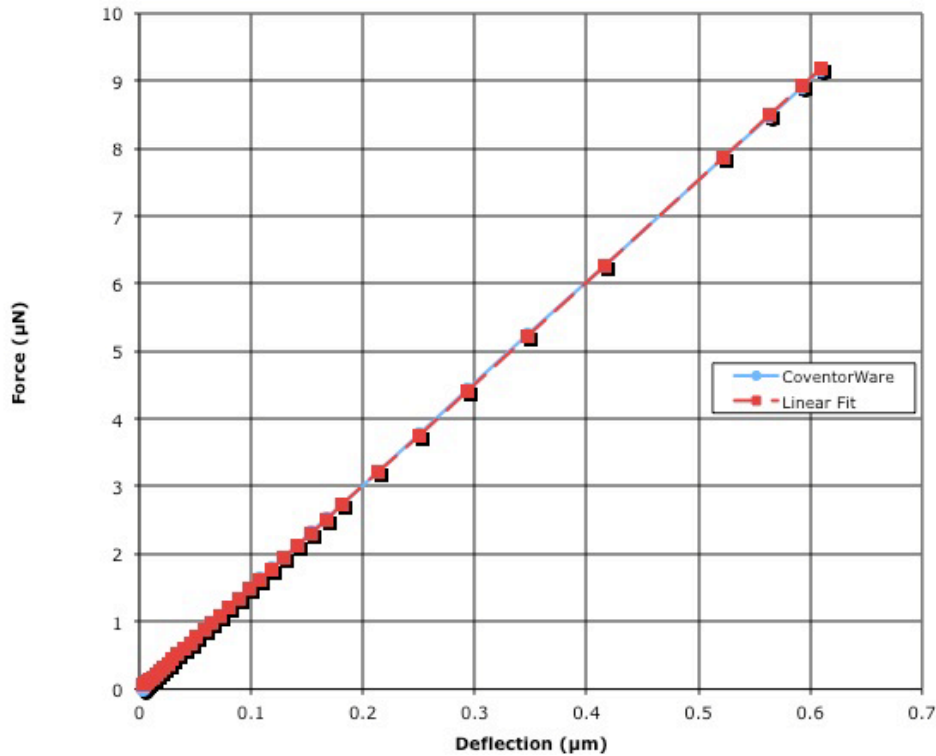


Figure 10: Simulated mechanical restoring force versus deflection;
effective $k=15.059$ N/m

coefficient of 0.9999. The latter quantity belies indication of a high degree of linearity of the line, as the regression calculation is dominated by a preponderance of points at small deflection, tending to be more linear. Divergence from the line increases with deflection, but in the domain of interest, the effect remains small enough to be neglected.

Several non-ideal mechanisms contribute to this discrepancy, one of which is the restoring force of the hinge connecting the flexure beam to the mirror plate. This hinge is $8 \mu\text{m}$ in the direction parallel to the length of the flexure (w), and $3 \mu\text{m}$ perpendicular (l), creating a $3 \mu\text{m}$ space between flexure and mirror. As the flexure deflects from the nominal height and the mirror descends, a torque is introduced in the hinge, which adds

to the mechanical potential energy of the flexure beams. This deflection is never more than 2% of the length L of the flexure, thus in the limit of small angles, the ratio of the vertical displacement to the flexure length approximates the angle over which the torque is applied. Assuming the force inducing the torque is applied perpendicularly to the lever arm (in this case, the flexure beam), the equation from [19] is modified:

$$\frac{1}{k} = \frac{1}{k_f} + \frac{1}{k_h} \quad (15)$$

where w is the width of the hinge as above; t the thickness ($2 \mu\text{m}$); E is Young's Modulus; l the length of the hinge as above; d the maximum distance of the flexure deflection; and μ is Poisson's Ratio for polysilicon (0.22 [67]). This equation models the hinge as another linear spring in series with the flexures, thereby adding a small, but non-zero, value of 0.013 N/m to the effective spring constant—the lumped model parameter—of the system.

Another stiffening effect is that of two-dimensional strain, commonly referred to as the plate effect. As the ratio of flexure width to length increases, so too does the curling of the beam in the axis of width, around the axis of length, creating what resembles a valley or half-pipe, with a curvature opposite in sign to that of the flexure deflection. The net result of this transverse curling is in effect to stiffen the flexure, and is usually modeled by use of a biaxial modulus in place of Young's modulus in the analytical beam-bending equations. This biaxial modulus is calculated by dividing the Young's modulus by difference of unity and Poisson's ratio of the material, and, since the latter is always less than one, the biaxial modulus is always greater than the Young's

modulus. The Euler-Bernoulli equations can be re-derived to remove this dependence on Poisson's ratio, allowing direct insight into the effect of the width-to-length ratio. As the width-to-length ratio for the system currently studied is 0.03, it is found [70] that the plate effect is likely not a source of deviation.

Another possible source of effective spring constant deviation is the increase of structural compliance if the design features built-up, pillar-like supports, such as the flexure beam anchors described for the current FMBD in Chapter 2. These supports are able to rotate in the presence of external moments induced by residual stress. It is found that this can be analytically modeled [70] as a small (relative to that designed) increase or decrease in mechanical flexure length. That is to say, a beam attached to an anchor that rotates behaves similarly to a slightly longer beam. Finite element modeling results and analytical estimations in [70] for maximum cantilever deflection versus several drawn mask lengths were plotted. It was found that the addition of 5.85 micron to the cantilever design length in the analytical equations fits the FEM data well. For this work, subtracting 5.85 micron to the nominal design length of 100 micron yields, via Equation (10), an expected mechanical spring constant of 15.069, within 10% of that simulated in CoventorWare. This structural compliance, combined with the addition of torsion spring action as described above, are then the dominant effects in deviating from the first-order estimation in Equation (10).

3.4. Parasitic Capacitance

This section serves to summarize modeling of the capacitance of micromirrors as simulated in CoventorWare. To start, the micromirror was simulated for input voltages

ranging from zero to pull-in, the latter being estimated by Coventor's pull-in detection algorithm. For each voltage, a total accumulated charge, deflection distance, and capacitance was recorded and exported. Excel was then used to tabulate the results for comparison to theory and fitting.

As an initial sanity check, the exported capacitance values were plotted against the ratio of accumulated charge and voltage for each input voltage, and found to match exactly. The former was then plotted against the familiar equation for the capacitance of infinitely long parallel conductors, employing the mirror plate area and exported deflection distances. Stark differences between the exported capacitances and theory were seen, both magnitude and rate of increase near the pull-in voltage.

A lumped parameter model was sought to include these nonlinearities, likely the results from neglecting the fringe field effects and capacitive contributions from the four flexure beams. This model was to take the form of the original, first-order equation for parallel plates, but using an effective area that would account for the aforementioned nonlinearities. Both this effective area model and that of exported capacitance were strongly nonlinear near the pull-in voltage and converge with increasing input voltage; the maximum divergence of 3.945 fF (roughly one order of magnitude smaller) occurs at 3.50 V. A misguided attempt to fit an analytical equation to this divergence curve resulted in a power law with a correlation coefficient of 0.997. This approach was abandoned due to complexity. Instead, a linear regression against the simulated capacitance versus gap data was performed and found to model more closely the difference between theory and observed capacitance over the range of gap values (Figure

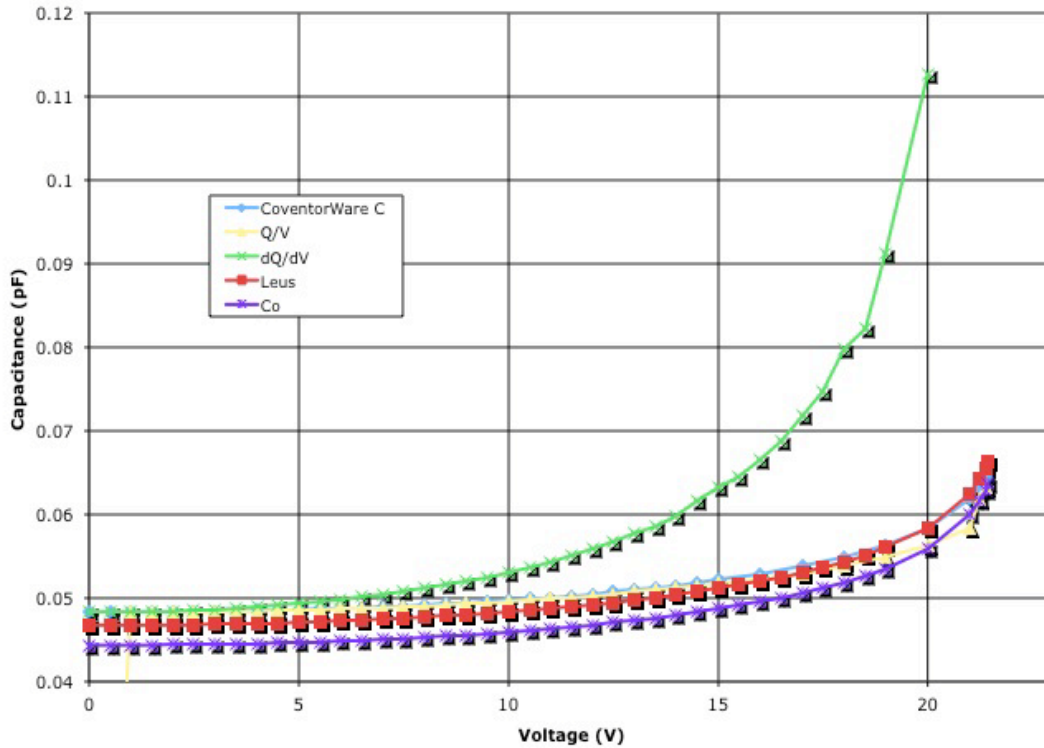


Figure 11: Simulated post-process capacitance; ratio of simulated total charge and voltage; differential charge over voltage ratio; Leus's fringe field corrected capacitance [71]; and basic parallel plate capacitance versus input voltage

11). The correlation coefficient for this linear fit was 0.9999. Separately, Microsoft Excel's linear least-squares regression function, LINEST, was used to fit a linear equation directly (in contrast to the difference curve above) to the exported capacitance versus the inverse of the exported gap, with y-intercept forced to zero. Dividing the fitted slope by the free-space permittivity yielded the effective area: $1.07 \times 10^{-8} \text{ m}^2$.

The contributions of fringe fields and the flexures were investigated in an attempt to explain observed differences between theory and simulation. First, the flexures deflect according to the Euler-Bernoulli equation (Equation (9)) presented in Chapter 2, and can

be considered as capacitors with one planar plate and one curved plate. Since the inverse of this equation is difficult to integrate analytically, an approach emulating a Riemann sum is taken to model the flexures as a series of parallel-plate capacitors, connected in parallel, with gap equal to the amount of deflection at that distance away from the fixed support. As this is a first-order attempt to quantify the order of magnitude of flexure capacitance, fringe fields, non-uniformities introduced by fabrication, and the fact that the ground plane is not directly below the flexure are ignored. The analysis proceeds by dividing the flexure into ten equal parts, calculating the deflection at the midpoint of each part to be used as the gap between plates, inserting this gap into the capacitance equation for parallel plates, and adding the contributions for the ten sections and four flexures. The resulting contribution is two orders of magnitude smaller than that of the mirror plate, and therefore may be neglected.

Fringe fields are modeled by previous work [71] in an analytical equation that accounts for non-zero plate thickness, side, and edge effects. The equation itself is a modified version of earlier work, the result of which is a Schwartz-Christoffel conformal mapping transformation describing the electric field with parallel-plate boundary conditions. What results underestimates the simulated capacitance at low voltages (larger gaps) and overestimates at high voltages (smaller gaps), but only by a maximum of three percent, outperforming both the basic parallel plate theory and the parallel plate equation linearly fitted effective area. This performance supports the need to consider fringe fields in an accurate treatment of the total capacitance.

The differential definition of capacitance, i.e., the ratio of the change in charge and the change in input voltage, is necessary as the basic theory for parallel plates assumes a static and uniform gap between the plates; since this gap has a voltage dependence (indeed, the modus operandi of electrostatic actuation), the differential definition of capacitance is more appropriate. To generate this differential data for comparison, a linear voltage trajectory was again applied to the device, offset from the original trajectory by 0.1 V, which enables a quasi-static differential analysis. As a second sanity check, this differential model and the original capacitance data were both plotted against input voltage and found to be strikingly dissimilar, providing some evidence for the inadequacy of CoventorWare's use of the steady-state definition of capacitance, which is the total accumulated charge divided by potential. CoventorWare obtains each of the values in this ratio by first inferring a surface charge on conductive surfaces based on changes in the electric displacement vector, and then integrating over the total surface area of the structure, yielding a total charge. The latter is then divided by input voltage and exported as a total capacitance. This can be seen by simply dividing the exported total charge by the known input voltage, which exactly follows the exported capacitance curve. The trouble with this approach is the relationship between the charge and the potential. The latter is defined, to first-order, as the strength of the electric field, E , set up between charges on the mirror plate and ground plane, multiplied by the distance between the charges, d , i.e., $V=Ed$. Since this device is electrostatically actuated, the accumulated charge interacts with this distance by design; in particular, a feedback loop is set up between the distance between the plates and the amount and

location of charge on each plate. To assume a constant distance is a mistake, the consequence of which is to ignore fundamental dynamics of the system. As such, the capacitance values given by CoventorWare will be considered suspect.

3.5. Fluid Damping

In order to characterize any film damping the micromirror might experience, a three-dimensional, one-quarter model of the mirror plate—with the remainder modeled by numerical continuity—is built in COMSOL Multiphysics simulator. A perfectly diffuse tangential momentum accommodation coefficient for the fluid is also assumed; this is reasonable based on work [69] on gas flows over pure silicon, which demonstrated diffuse accommodation despite orders of magnitude smoother surfaces. Slip flow was

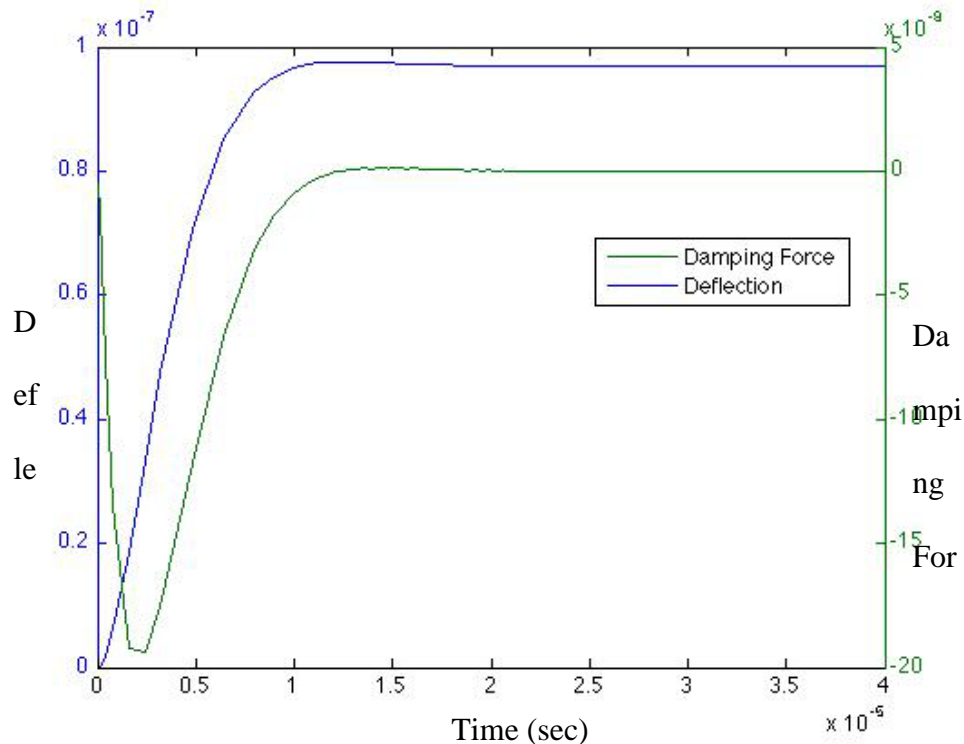


Figure 12: Damping force (N) and mirror deflection (m) vs. time (s)

accounted for in the simulation as well, since the system has a Knudsen number of 0.034. A constant potential is specified across the mirror and ground plates, and the simulation is conducted to record the transient response of all applicable physical forces: mechanical, electrical, and fluid (Figure 12). The velocity of the plate at each sample period is calculated numerically in post-processing using a simple difference function in MATLAB. The COMSOL-calculated damping force is then divided at each sample period by the plate velocity to generate an estimate of the damping coefficient, B , at 1.1885×10^{-5} Ns/m. As the plate settles to equilibrium, the velocity oscillates around zero, causing the estimate of B to vary severely; as such, only a small subset of samples around the maximum velocity are used to calculate B , as they displayed the most stable velocity values.

3.6. Transient Analysis

The above analyses quantify various physical characteristics required to describe the FBMD with a system-level model, which will be directly employed by the Kalman Filter (developed in Chapter 4) to estimate unobservable states—specifically, and for reasons outlined in Chapter 1, the deflection of the mirror plate. As deflection and potential are interdependent upon each other and demonstrate strong, nonlinear transients, these characteristics are simulated together to verify the claims of stability in Section 2.7 that were based on simple, static models. The results are shown in Figure 13. Despite beam and fluid damping transients, delays for charge accumulation (albeit minute), and all the nonlinearities described above, the results indicate stable equilibria are possible up to just over 18.3 Volts. This value is decidedly close to the analytically derived value of

18.4 Volts in Chapter 2, but assumes perfect polysilicon edges and does not account for the “bump” in each of the flexure beams as CoventorWare does. Beyond the sanity check, the transients also indicate that stability is reached within 15 to 20 microseconds, and, depending on the magnitude of the input, instability begins running away before 40 microseconds. This implies the sample rate of the controller must be 50 kHz to meet the Nyquist criterion, and 250 kHz for a margin of ten samples on the transient.

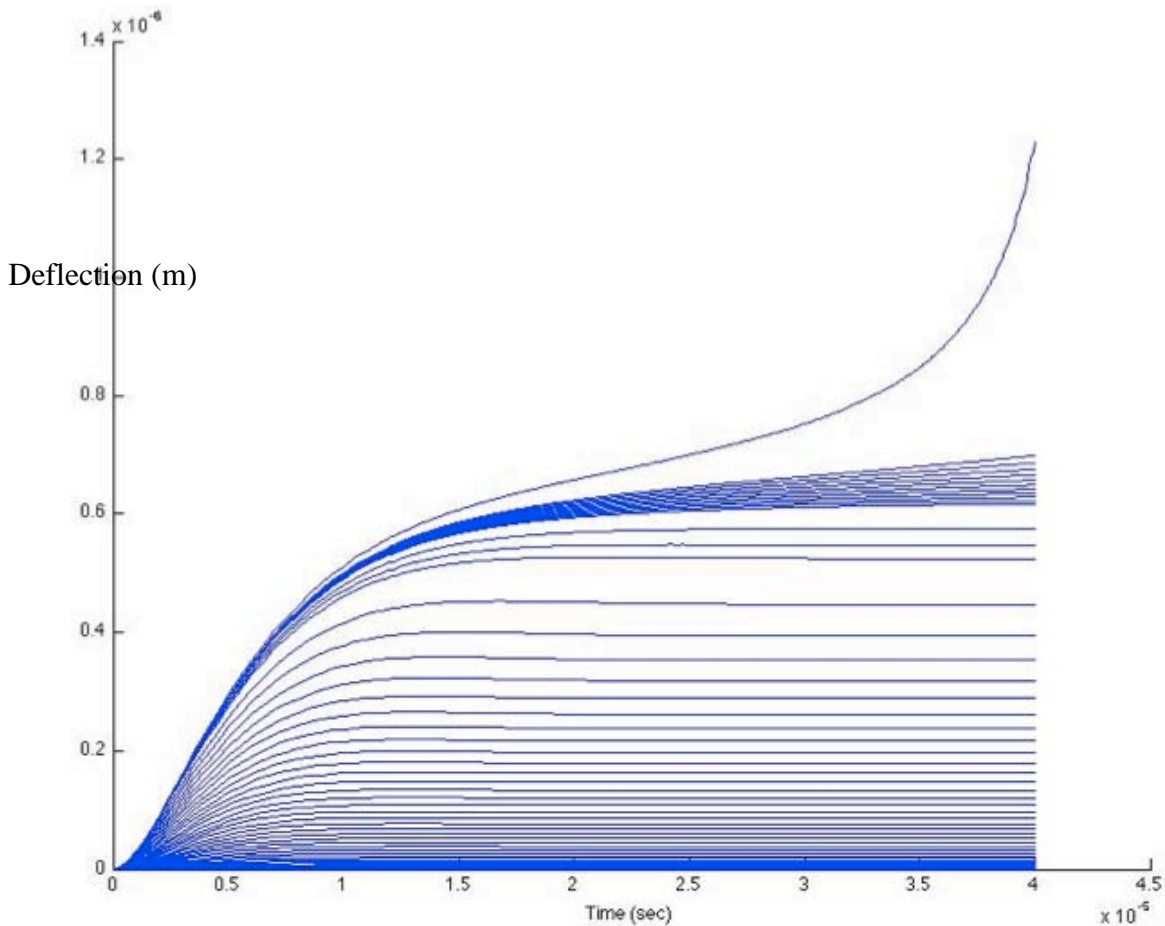


Figure 13: Mirror plate deflection (m) vs. time (s) via COMSOL. Input voltage swept from zero to 18.34 V (top, diverging trajectory).

4. State Estimator and Controller Design

4.1. Chapter Overview

This chapter describes the designs for the observer and controller algorithms, to include assumptions made in the measurement process, and concludes with an overall algorithm description. It is split into three interdependent parts: the first for the observer, the second for the controller, and the third for the algorithm description. The first part concludes with process equations used for the observer. The second section concludes with the control law equations. The last part steps through the MATLAB scripts that execute the first two parts.

4.2. State Estimator Design

The controller requires an accurate estimate of the controlled variable to be effective. The observer, as such, is the lynchpin to effective control, as it provides an estimate of the controlled variable in spite of indirect observation and noise. This section describes the design of a Kalman Filter to be applied to the FBMD as analyzed in previous chapters.

4.2.1. Measurement Design and Assumptions

Using parallel-plate capacitor charge accumulation and mirror plate dynamics relationships developed in Chapters 2 and 3, the observer infers a mirror plate deflection from measured changes in voltage across the mirror. The proposed measurement system is modeled as an ideal voltmeter, to include an internal resistance of 1 M Ω . This design is motivated by the ease of implementation in a lab for empirical verification, and is

demonstrative of a general system of electrical measurement. To obtain the voltage across the FBMD, the mirror is driven by the series connection of an ideal voltmeter (in particular an independent voltage source and an internal resistor) and the FBMD. The Norton equivalent of this circuit is employed (Figure 14), making the calculation of the amount of current going to the FBMD a simple application of Kirchoff's Current Law (KCL): the current to the FBMD is the difference of the current source (control signal) and the current through the internal resistor. Since the current through the FBMD is the time-differential of the voltage across it scaled by the effective capacitance at that instant (Equation (16)), the observable state variable is obtained as the integral of the difference of the control signal and the resistor current, divided by the effective capacitance at that moment:

$$\text{---} \quad \text{---} \quad \text{---} \quad (16)$$

$$\text{---} \quad \text{---} \quad \text{---} \quad (17)$$

Modeling the FBMD as a voltage-controlled capacitance in this way assumes that the

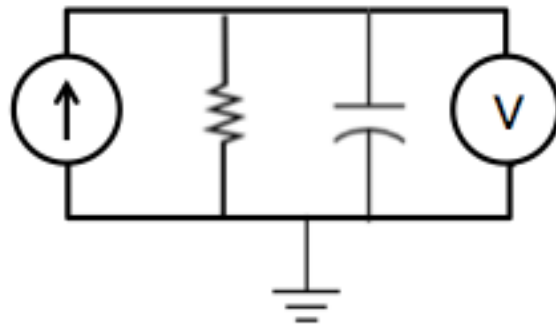


Figure 14: Norton-equivalent driving circuit. FBMD shown here as a capacitor.

capacitance is linear, allowing the time derivative of the capacitance to go to zero.

As this observer will be implemented digitally, the voltmeter will sample the voltage across the FBMD and hold for one sample period. This process is repeated every 50 nanoseconds, modeling a voltmeter capable of 20 MHz operation. The voltmeter is subject to thermal drift and imprecisely known internal resistance, but performs no filtering or buffering of more than one sample. Other sources of noise (shot noise, cross-talk, etc.) may be added with appropriate models; for generality, the noise in the filter algorithm is modeled as additive, white, and Gaussian, with a magnitude of 0.01 and mean of zero.

In this work, measurements are generated in software by the MATLAB script `get_meas()`. Inputs to the script include absolute start and stop times (the products of the sample period and the previous and current sample numbers), the previous measurements, and the previous control signal, the script outputs the current sample period's measurement of voltage across the FBMD, as well as the gap measurement for troubleshooting. The script calculates the measurements using MATLAB's `ode45` script and the nonlinear functions developed in Chapter 3, with the boundary conditions specified by the time period taken as input by `get_meas()`, initial state, and control signal. This implementation allows for changing control signals in real-time, at the severe cost of calling `ode45()` for each sample period; pre-calculation of the control history would speed up the script significantly by enabling the measurement history to be pre-calculated and called as a look-up table. This, however, would not be representative of a real-time controller implementation.

4.2.2. Propagation Design

With the measurement system described in the previous section, and equations of motion analyzed in Chapter 3, the following state dynamics equations describe using nonlinear, first-order partial differential equations the system states as potential across mirror plates, mirror deflection, and mirror velocity:

$$\begin{matrix} \text{-----} & \text{-----} \\ & \\ \text{-----} & \text{-----} \end{matrix} \quad (18)$$

The state noise covariance, quantified by the matrix \mathbf{Q} , indicates the uncertainty in the dynamics equations. Real-world disturbances, such as drift, wander, and non-white noise, would require additional states modeled by shaping filters driven by white Gaussian noise. In this work, no assumptions may be made about the deployed environment; rather, pseudo-noise is added the dynamics equations in an attempt to account for unmodeled effects. \mathbf{Q} can be adjusted to accommodate unexpected disturbances and system model inadequacies, such as the consequences of linearizing dynamics equations of higher polynomial orders. The loss of the effects of higher order terms may be conceptually considered by the algorithm as an unmodeled disturbance and negotiated in the same way, by increasing the state noise covariance \mathbf{Q} . This increase has the effect of adding weight to the measured state value over the propagation calculation in the observer algorithm, desirable during the initial transient or large disturbances. Too much weight on measurements vice calculated estimates can be detrimental to a detectable system. The measurement improves the estimate of the controlled variable

(FBMD deflection) using a voltage in conjunction with modeled dynamics; too little weight on the latter creates systemic errors that the Kalman Filter has no means to remove. By trial and error, it was found that values of 1×10^{-4} , 1×10^{-9} , and zero along the diagonal of \mathbf{Q} (roughly 0.1% of each expected state magnitude) provided a good compromise.

Pursuant to the assumption that small deviations from system equilibrium can be treated as linear, the dynamics equations are linearized before discretization. Equations for equilibrium state and control values are found as functions of the desired setpoint by setting the dynamics equations to zero and solving for each state and for the control signal:

$$\begin{aligned} \mathcal{X}_0(y_d) = \mathbf{x}_0 &= \begin{bmatrix} u_0 * R_{mt} \\ y_d \\ 0 \end{bmatrix} \\ u_0(y_d) = u_0 &= (g_0 - y_d) * \sqrt{\frac{2k_s y_d}{e_0 A R_{mt}^2}} \end{aligned} \quad (19)$$

The dynamics equations are linearized by calculating the Jacobian and setting the states and control signal to their respective equilibrium values per equations previously described:

$$F = \left. \frac{\partial \mathbf{f}}{\partial \mathbf{x}} \right|_{\mathbf{x}=\mathbf{x}_0, u=u_0} \quad B = \left. \frac{\partial \mathbf{f}}{\partial \mathbf{u}} \right|_{\mathbf{x}=\mathbf{x}_0, u=u_0} \quad (20)$$

$$\begin{matrix} \text{-----} & \text{-----} \\ \text{-----} & \text{-----} & \text{-----} \end{matrix} \quad (21)$$

$$\text{-----} \quad (22)$$

\mathbf{Q} is as described in the previous section, and \mathbf{G} is set to the identity matrix. These matrices, \mathbf{F} , \mathbf{B} , \mathbf{G} , and \mathbf{Q} , along with the sample period Δt , are input to the equiv_discrete() script, which employs the MATLAB c2d() function to generate a discretized state dynamics matrix, Φ , control matrix \mathbf{B}_d , and state dynamics noise matrix \mathbf{Q}_d , from respective continuous equations, each of which are used to propagate the estimate of state in the Kalman Filter from one sample period to the next.

Initial conditions for each filter simulation are assumed to be at quiescence, in this case, zero for all states and control. In this case, MATLAB finds difficulty numerically solving the differential equations starting at pure zero, thus “near” zero values of 1×10^{-15} are used instead. The state covariance matrix \mathbf{P} has an initial value of 10 along the diagonal. This value was found by trial and error to have an appropriately small transient behavior.

4.2.3. Truth Generation Algorithm

Filter performance may be judged by analysis of residuals and error history. Residuals are calculated by the difference of the measured values and post-propagation state estimates mapped to measurement space. As described above, the measured values

are not empirical data, but rather are simulated by periodic solutions to nonlinear, ordinary differential equations (ODE)—the same equations from which the filter’s dynamics model are linearized. Although residual analysis is typically very useful, it merely serves in this case to indicate how well the linearized filter predicts the output of a more robust ODE solver. Error history analysis is essential in this case, and requires a dataset to act as truth for comparison.

The FEM analysis as executed in COMSOL serves as this dataset. As described in Chapter 3, the FBMD system analysis consisted of setting each plate of the FBMD at a constant potential and recording the time history of charge accumulation and mirror deflection. By contrast, the filter applies a known (not necessarily constant) current and measures the change in voltage over time. Furthermore, the FEM and filter time vectors do not overlap. This disparity is overcome by considering the FEM dataset as a look-up table, with `geterr()` as a look-up script, rather than a directly analogous deflection trajectory to be compared point-for-point with the observer’s results. The raw FEM data is first organized into structured arrays by electrical potential, while removing redundant data necessary for FEM accuracy. The MATLAB `timeseries` command is employed to create, for each FEM-simulated electrical potential, a time trajectory of maximum mirror deflection, with which the `resample` command is used to match observer and FEM time vectors. `Resample` introduces some small amount of error in the data, as it estimates data by linearly interpolating between times in the FEM data to align with those in the observer. Once the FEM data are resampled along the observer’s time vector, `geterr()` calculates the total charge accumulated on the FBMD plates for each time sample, then

for the same voltage finds the charge and deflection as determined by the FEM. The difference of FEM and observer charge and deflection values for each time is output as the error array.

4.3. Controller Design

The central goal of this work is to mitigate mirror snap-in and demonstrate controlled deflection of the FBMD throughout the gap. To this end, the deterministic control law sought will achieve and maintain (requiring type-1 for modeling errors) a desired non-zero setpoint, and reject disturbances. Typically, one or more system-level performance requirements would be levied to guide the control design. For example, consider a free-space optical communications system employing an array of FBMDs for wavefront error correction; characteristics such as deflection accuracy of +/- 1 nm, 1 ns response time to steady state, and 10% overshoot may be necessary for an acceptable bit error rate, enabling mission success. In this work, design choices were made primarily to mitigate snap-in, but system-level considerations will be indicated throughout the design description.

4.3.1. Pseudo Rate Δu

One means to effect integral control is to cost not only differences in control signal from the nominal u_0 calculated above, but also differences between samples in time. The state vector \mathbf{x} is augmented by δu , quantifying the former, and introducing as the control signal Δu , each defined respectively by the following equations:

$$\begin{aligned}\Delta u(t_i) &= u(t_i) - u(t_{i-1}) \\ \delta u(t_{i+1}) &= \delta u(t_i) + \Delta u(t_i)\end{aligned}\quad (23)$$

In so doing, both δu and Δu carry weights in the cost equation, constraining both appropriately with respect to system performance requirements.

4.3.2. Cost Assignment

The \mathbf{X} , \mathbf{U} , and \mathbf{S} matrices quantify costs for state, control, and cross-terms, respectively, in the infinite horizon cost equation \mathbf{J} , introduced in Chapter 2. As described above, the state vector is augmented by δu , so \mathbf{X} is a 4 by 4 matrix, declared in software in four parts. The first declared, \mathbf{X}_{11} , is a 3 by 3 matrix and defines costs for the system states. Since the pull-in voltage was found by FEM to be 18.36 volts, the cost assigned is 0.0025 (the inverse of the square). Similarly, the maximum deflection is 2 microns, so the cost is set as 2.5×10^{11} . Last, the velocity cost is set at unity, with the goal of minimizing velocity directly. \mathbf{X}_{12} , as a scalar cross-term, sets the cost weight for between-sample dynamics of a continuous plant not captured by a discrete observer and controller combination. Since the samples are taken 35 times faster than the characteristic time constant of the unforced system (modeled as a damped harmonic oscillator), the consequences of not considering interstitial time periods in the cost minimization is assumed to be negligible, and \mathbf{X}_{12} is concordantly set to zero. \mathbf{X}_{22} is the cost weight on control deviations from the nominal control u_0 and is a scalar. In `getGc()` (described in the next section), this is a function of u_0 , effectively setting \mathbf{X}_{22} as the inverse square of 20% of u_0 . Similarly, the cost weight of the control pseudorate Δu is quantified by \mathbf{U} and is defined initially as 1×10^4 , to model a maximum current output of the controller is 10 mA (later tuned to 1×10^3 to allow a more robust response). Finally, \mathbf{S} is set to zero using the same reasoning as \mathbf{X}_{12} .

4.3.3. Dlqr to Get G_c

Having augmented the state transition matrix Φ and discrete control injection matrix B_d to reflect the state augmentation described in the previous section, and defined the cost matrices X , U , and S , getGc() then calls the MATLAB script for discrete linear quadratic regulator calculation, dlqr(), passing each of these matrices as inputs. dlqr(), for Discrete Linear Quadratic Regulator, calculates regulator gains that minimize the quadratic cost function specified earlier, as well as the infinite horizon solution of the discrete-time Riccati equation. Using dlqr() here implies the assumption of certainty equivalence; that is, contributions from noise sources are not taken into account in the regulation problem. Assuming the inputs pass dlqr requirements for a closed solution (Φ and B_d must be stabilizable; X and U positive definite; and no unobservable modes in the unit circle), getGc() outputs the dlqr() solution for G_c .

4.3.4. Dynamics Embedding via Π , K_x and K_ξ

With regulator gains in hand, effort is now spent ensuring that the controlled variable y_c drives the equilibrium to the desired setpoint y_d :

$$\begin{bmatrix} (\Phi - I) & B_d \\ C & D_y \end{bmatrix} \begin{bmatrix} 0 \\ y_d \end{bmatrix} \quad (24)$$

Assuming the dimensions of u and y_c are equal, and the left-hand matrix is invertible, Π is defined [62] so as to solve for an equilibrium solution as a function of y_d :

$$\begin{bmatrix} \mathbf{x}_0 \\ u_0 \end{bmatrix} = \begin{bmatrix} (\Phi - I) & B_d \\ C & D_y \end{bmatrix}^{-1} \begin{bmatrix} 0 \\ y_d \end{bmatrix} = \begin{bmatrix} \Pi_{11} & \Pi_{12} \\ \Pi_{21} & \Pi_{22} \end{bmatrix} \begin{bmatrix} 0 \\ y_d \end{bmatrix} \quad (25)$$

Perturbation variables may now be defined as deviations from these equilibrium values:

$$\begin{aligned}
\delta \mathbf{x} &= \mathbf{x}(t_i) - \mathbf{x}_0 = \mathbf{x}(t_i) - \Pi_{12} y_d \\
\delta u &= u(t_i) - u_0 = u(t_i) - \Pi_{22} y_d \\
\delta y_c &= y_c(t_i) - y_d
\end{aligned} \tag{26}$$

These perturbation variables are passed to the cost equation J , and \mathbf{X} , \mathbf{U} , and \mathbf{S} contain weights appropriate for perturbation, rather than for the full state values. In this way, the canonical LQ regulator equation, introduced in Chapter 2, is defined in terms of perturbation variables, in which the definitions of the perturbation variables can be substituted to produce a type-0, nonzero setpoint controller [62]:

$$\begin{aligned}
u(t_i) &= u_0 - \mathbf{G}_c(t_i) [\mathbf{x}(t_i) - \mathbf{x}_0] \\
&= -\mathbf{G}_c(t_i) \mathbf{x}(t_i) + [\Pi_{22} + \mathbf{G}_c(t_i) \Pi_{12}] y_d
\end{aligned} \tag{27}$$

As a type-0 controller, this equation ensures that the system will settle to *an* equilibrium, though not necessarily with zero steady-state error, i.e., to y_d ; inevitable modeling errors cause imprecision in Π , creating steady-state errors. As such, a term proportional to the total regulation error is motivated. It can be shown that embedding the system dynamics into the controller gains, and specifically adding a signal to the perturbation controller proportional to the regulation error, provides the type-1 characteristic necessary to accommodate regulation errors [62]:

$$[K_x \quad K_\xi] = [\mathbf{G}_{c1} \quad \mathbf{G}_{c2}] \begin{bmatrix} \Pi_{11} & \Pi_{12} \\ \Pi_{21} & \Pi_{22} \end{bmatrix} \tag{28}$$

$$u(t_i) = u(t_{i-1}) - K_x [x(t_i) - x(t_{i-1})] + K_\xi [y_d(t_i) - y_c(t_{i-1})] \tag{29}$$

4.3.5. Description of Control Flow

A block diagram of the controller is shown in Figure 15. Before the initial time t_0 , the system is assumed to have reached steady state; here, the system starts at quiescence. At t_0 , y_d changes from $y_{d,old}$ to y_d , which sets the initial control signal proportional to the regulation error, as the first and second terms of Equation (24) are zero at t_0 . Using the propagate and measurement processes described above, the Kalman Filter produces a refined state update (and residuals for diagnostics as motivated in Section 2.8), which is passed to the deterministic PI controller. The controller revises the control signal and applies the signal simultaneously to a sample-and-hold memory buffer and the FBMD itself (the latter only being modeled via `get_meas()` and `geterr()`). At the start of the next sample period, the process repeats itself.

4.4. Script Implementation

This section serves as the end-to-end description of the algorithm (see Appendix), tying together subroutines detailed in previous sections. The main script begins by

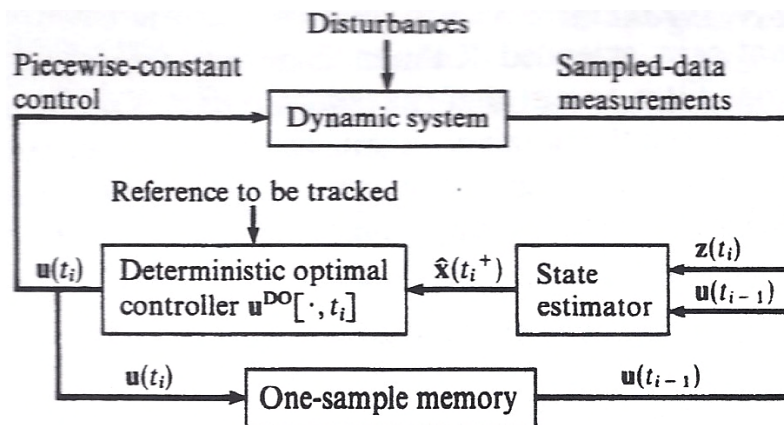


Figure 15: Controller block diagram assuming certainty equivalence [62]

declaring physical constants, sampling frequency, and sample vector length. State and measurement noise covariance magnitudes are set next, and are followed by translation matrices \mathbf{H} and \mathbf{C} , which map states to measurement space, \mathbf{z} , and controlled variable space, y_c . The desired deflection, y_d , is declared next and used to calculate $\mathcal{X}(y_d)$ and $\mathcal{U}(y_d)$. These latter values are used as the linearization nominal for the Jacobian matrices \mathbf{F} and \mathbf{B} , which are discretized by the sub-script equiv_discrete() to produce outputs Φ , \mathbf{B}_d , and \mathbf{Q}_d . As described above, the system dynamics model, in the form of Φ and \mathbf{B}_d , is embedded in controller gains via calculation of $\mathbf{\Pi}$. The subroutine getGc() is called next and outputs controller gains associated with the infinite horizon linear quadratic regulation problem, as described above and as solved by MATLAB's dlqr() routine. The final controller gains, \mathbf{K}_x and \mathbf{K}_ξ , are calculated using the formulas above.

MATLAB suffers speed penalties for variable-sized arrays, such as those that expand with every sample. To mitigate this penalty, \mathbf{x} , \mathbf{P} , \mathbf{z} , u , and the residual matrices are preloaded as zero matrices of length equal to the sample history length, as declared at the beginning of script. Last declarations are the filter initial conditions: the state vector \mathbf{x} is assumed to start from quiescence; the first control signal is calculated using the control law derived above; and the initial covariance matrix \mathbf{P} is found by trial and error to be $10 \times \mathbf{I}$.

The Kalman Filter proper, here instantiated as a *for* loop, starts by propagating the state vector and covariance matrix one sample forward. This is followed by the “update” process begins by calculating the denominator of the Kalman gain, \mathbf{A} , which will be used later in the script for visualization of the residuals. After the Kalman gain K , a scalar, is

calculated, `get_meas()` is called to obtain the discrete measurement \mathbf{z} , and from it the state estimate mapped to measurement space (the product of \mathbf{H} and \mathbf{x} , effectively retaining the first state) is subtracted to produce the residual. This residual—the difference of the estimated and measured voltage across the FBMD—is scaled by the Kalman gain and added to the state estimate to produce the “updated” state estimate. The covariance matrix is updated as well by subtracting the product of K , \mathbf{H} , and \mathbf{P} from \mathbf{P} . The last step in the *for* loop is calculating the deviation of covariance by taking the square root of the diagonal of \mathbf{P} . This *for* loop repeats for the entire length of the time history declared at the beginning of the script.

Upon completion of the *for* loop, a matrix of error values quantifying the difference between truth, as defined above, and the observer’s estimate for each sample period is initialized and calculated using the `geterr()` subroutine. Finally, the script produces two figures as visualizations of performance. The first figure contains two subplots with the time history of voltage and deflection errors, respectively, and deviation bounds. The second figure plots the time history of residuals and confidence bounds.

5. Results and Conclusions

5.1. Introduction

This chapter presents and discusses the results of applying the KF and LQ controller developed in Chapter 4 to the FBMD introduced in Chapter 1 and analyzed in Chapters 2 and 3. The first section discusses the KF performance, to include analysis of the residuals and errors from the truth model. The next section presents the successful control of FBMD past one-third of the gap. Conclusions follow this section, and the chapter finishes with suggestions for future work.

5.2. Observer Results

The linearized KF presented in Chapter 4 was first employed with various constant control inputs, and then with the LQ controller also developed in Chapter 4. The modeling software suites themselves imposed the largest difficulty. COMSOL does not do well in simulating simple circuits in conjunction with a multiphysics model, and just the model alone did not allow for the simulation of circuitual charge flow as a result of conservation of energy. With no current, all COMSOL simulations, herein used as truth data, were conducted with the mirror plate and ground held at constant potential. The key point is that the MATLAB script, in simulating the observer design, allows for a varying potential across the FBMD with a constant Norton-equivalent applied current, whereas the COMSOL simulations are exactly opposite. The end result is that, while the filter is tuned to minimize residuals and maintain a residual mean around zero, the error with respect to “truth” results are less definitive.

Filter performance is tuned primarily through adjustment of the measurement noise covariance and secondarily through adjustment of the filter noise covariance. The first simulation takes as input a constant current of 10 μA , which results in 10 volts steady-state across the FBMD and a deflection of 97 nm. The observer is linearized around the analytical equilibrium state and control values. Figure 16 shows that the state estimates are accurate and well-behaved, while Figure 17 demonstrates the residuals are steady, small compared state values, and centered about zero.

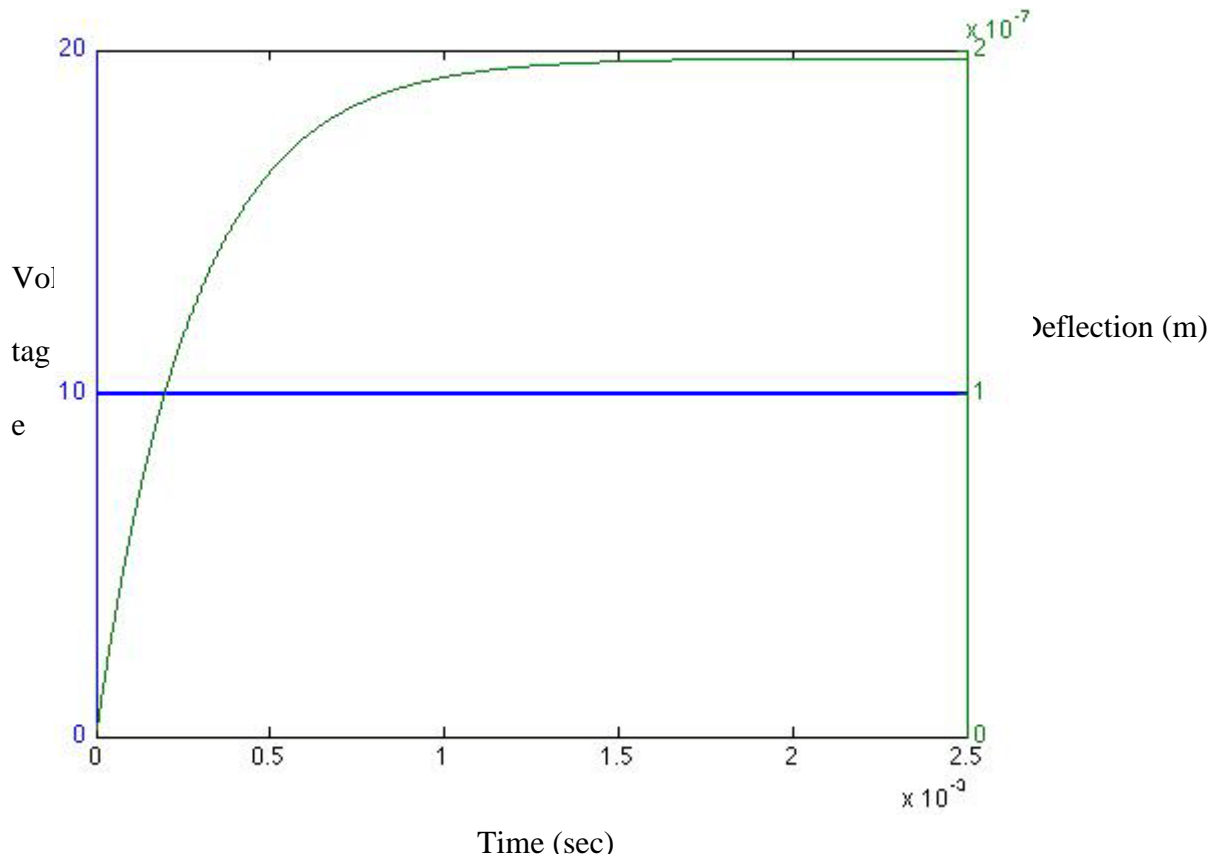


Figure 16: Voltage across FBMD in blue (V) and deflection in green (m) vs. time (s)

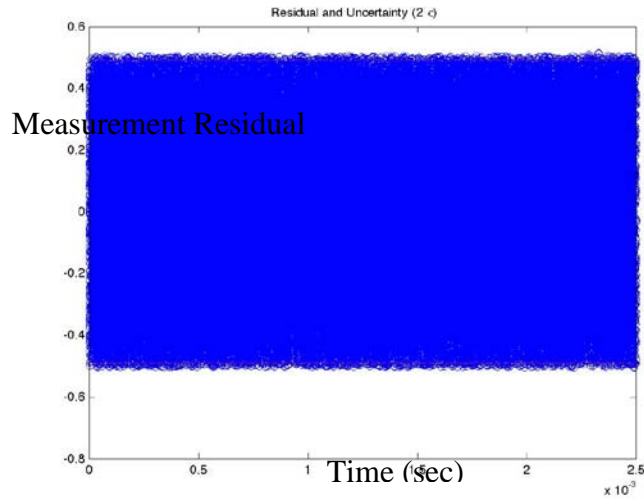


Figure 17: Residuals and filter-calculated uncertainty in dashed lines vs. time; constant input at 10 uA

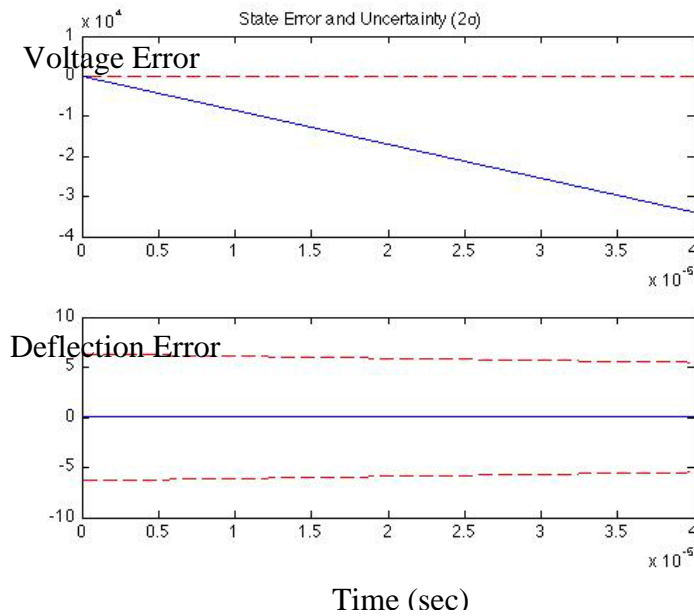


Figure 18: Top graph shows observer error in estimate of voltage; bottom graph error in estimate of deflection. Constant input of 10 uA. Diverging voltage error is an anomaly of `get_err()`.

The second simulation shown takes as input a constant current of $11.29 \mu\text{A}$, which analytically corresponds to an equilibrium deflection of $1.5 \mu\text{m}$. Figure 19 demonstrates the snap-in very clearly, as the deflection (shown as the green line) increases asymptotically. Residuals and filter-computed uncertainty in Figure 20 are increased on average over the previous case, but remain steady and centered about zero; this implies that, despite being in an unstable operating point, the linearized model holds as valid. The error plots in Figure 21 demonstrate the shortcoming of the `geterr()` script; since the COMSOL simulation produced no deflections of $1.5 \mu\text{m}$, the lack of data manifests as accumulating error and diverging covariance.

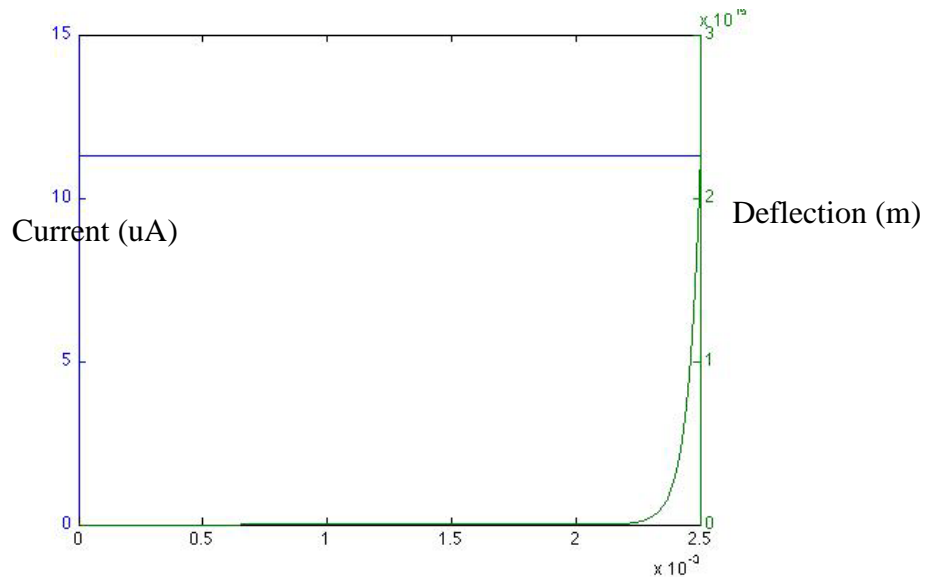


Figure 19: KF estimate of voltage across FBMD (blue, in V) and rapidly diverging deflection (green, in m) vs. time (s) for constant input current of $11.29 \mu\text{A}$

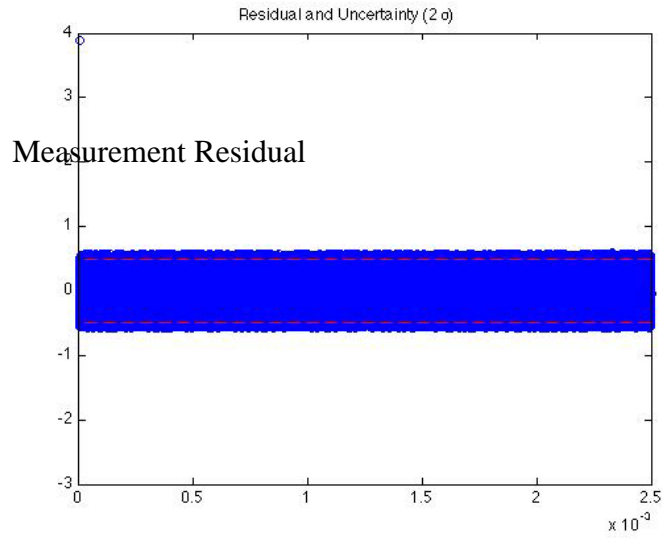


Figure 20: KF-calculated residuals and uncertainty for constant input of $11.29 \mu\text{A}$

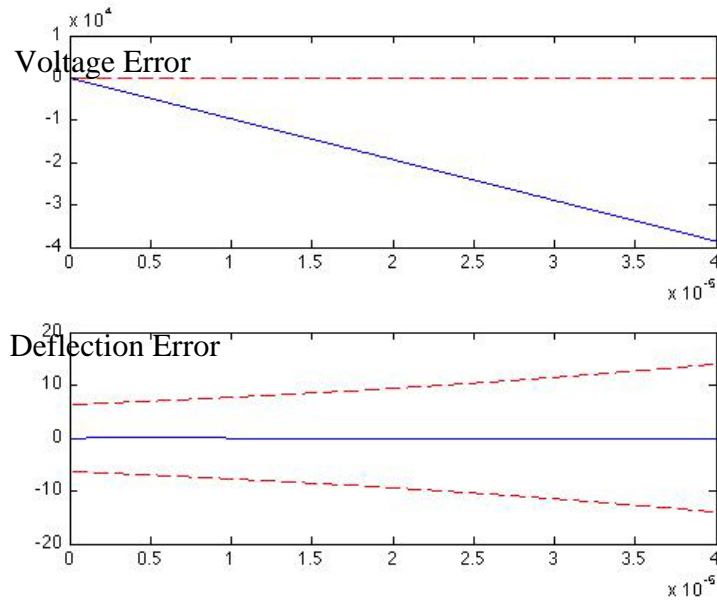


Figure 21: Errors in estimate of voltage across FBMD (top) and deflection (bottom) vs time. Note the divergence in deflection confidence, corresponding to the divergence of the system.

5.3. Controller Results

With a working linearized KF, the LQ controller is implemented and analyzed. The following set of figures show reaching and maintaining desired deflections of $1.0\ \mu\text{m}$ and $1.5\ \mu\text{m}$, respectively—each well beyond one-third of the gap.

Figure 21 shows the deflection and control signal resulting from setting the desired deflection y_d to 1 micron. The mirror deflection is smooth and stable, with no overshoot

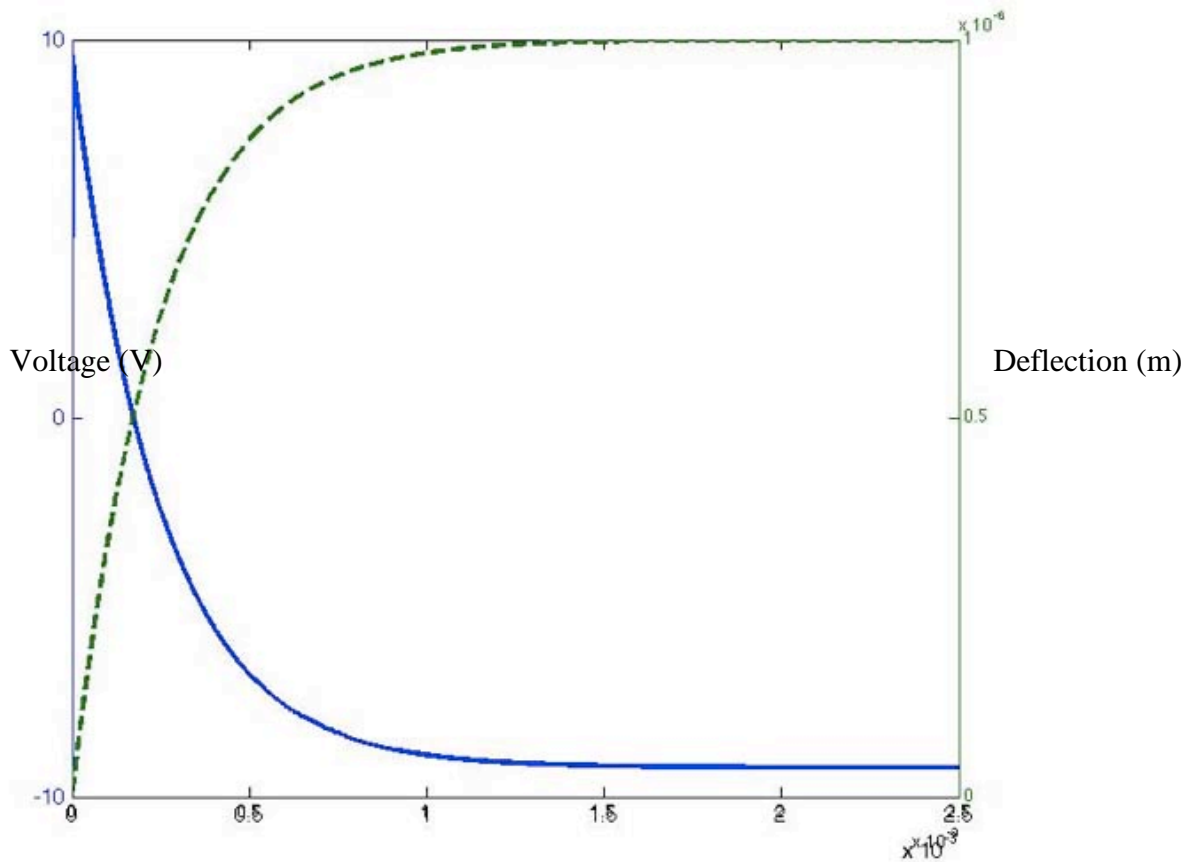


Figure 22: Voltage across FBMD (V, in blue) and deflection (m, in green) vs. time. The FBMD achieves a steady deflection of $1\ \mu\text{m}$.

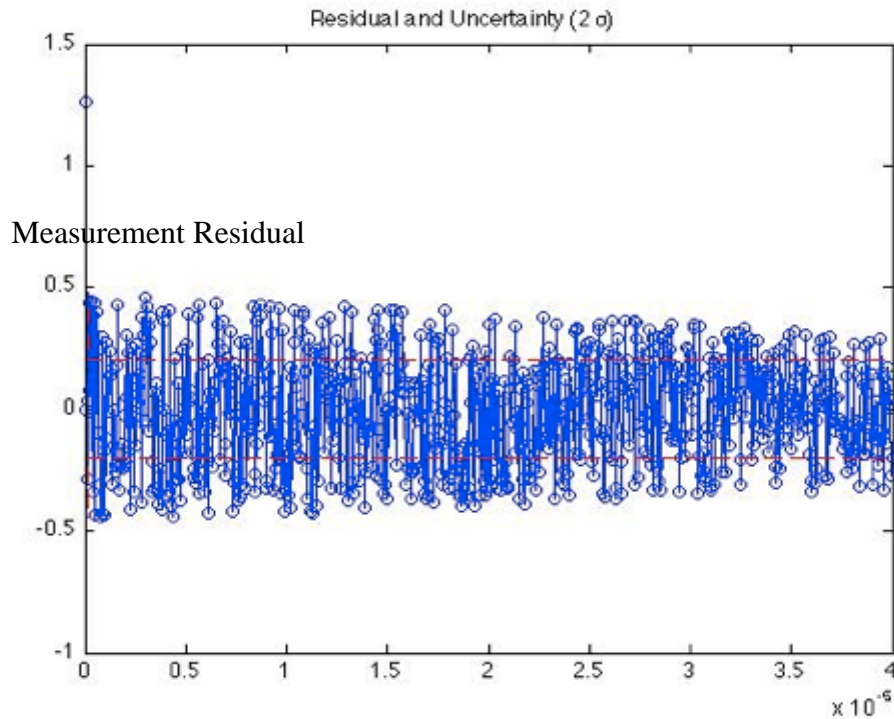


Figure 23: Residuals and filter-computed uncertainty for $y_d=1.0 \mu\text{m}$, tuned liberally (i.e., \mathbf{Q} set “optimistically” or less than actual model error).

and a rise time of 1 millisecond. Interestingly, the controller changes polarity just before the deflection reaches the point of instability at one-third of the quiescent gap, g_0 . Figure 22 shows the residual data for the first observer state (voltage across the FBMD) and filter-computed covariance. As delineated in Section 2.8, model adequacy is reflected by the steady covariance, lack of bias in the residuals, and low root-mean-square value relative to the magnitude of the steady-state control signal. However, the covariance curves fail to encapsulate the residual data, but rather are less than the absolute peak values of the residual data. This implies that the KF is underestimating the variance of the data, which may be mitigated by increasing the dynamics noise strength \mathbf{Q} .

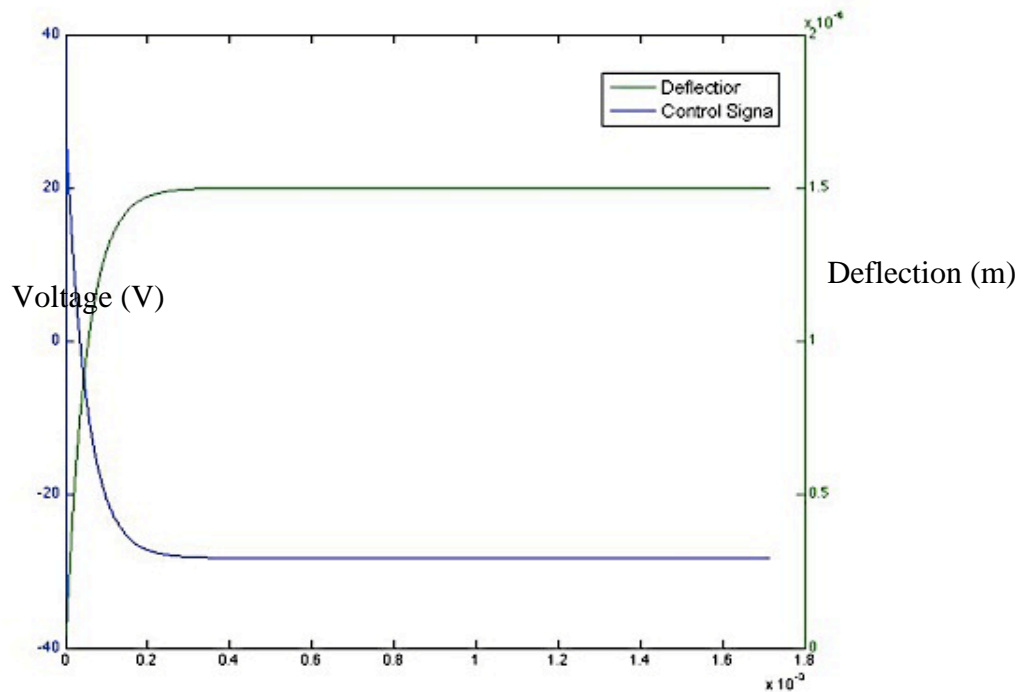


Figure 24: Voltage across FBMD (V, in blue) and deflection (m, in green) vs. time (sec) for $y_d=1.5 \mu\text{m}$

For the case in which the desired deflection y_d is set to 1.5 micron, the resulting control signal, deflection, residual data, and covariance are shown as before in Figure 23 and Figure 24. Figure 23 shows successful deflection through three-quarters of the gap, smoothly reaching equilibrium in 0.2 milliseconds without overshoot. As before, Figure 24 shows that the filter is tuned optimistically and underestimates the covariance. A key difference between Figure 24 and Figure 22, however, is that the residuals start much higher, but as equilibrium is established, the residuals reduce to a level closer to the KF's estimate.

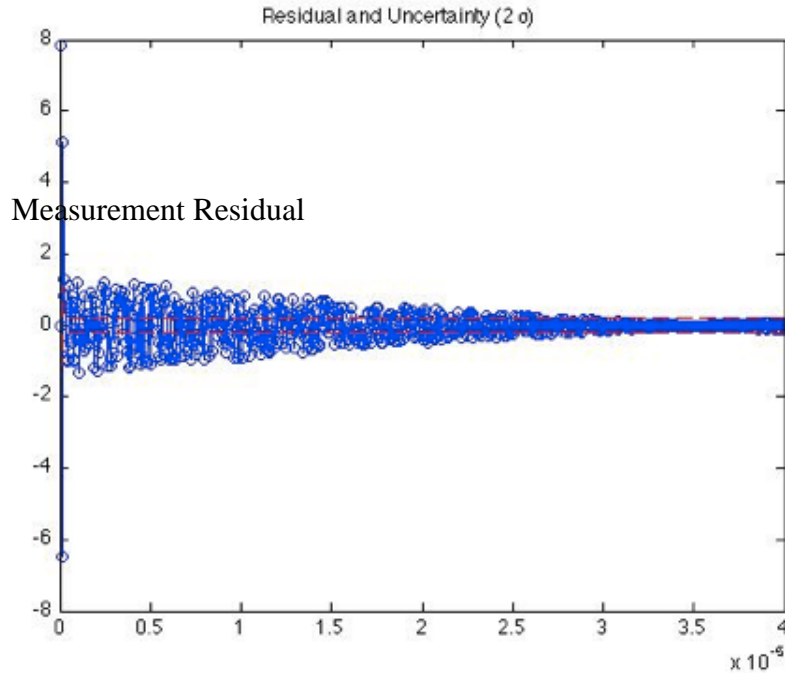


Figure 25: Residuals and filter-computed uncertainty for $y_d=1.5 \mu\text{m}$, tuned liberally.

5.4. Conclusions

The KF-based, LQ control implementation for an FBMD application is shown to be able to achieve and maintain deflections beyond the theoretical snap-in point at one third of the gap. The implementation here is well suited for digital implementation, and eminently extendable to an array of FBMDs. Deflection inference via electrical measurement has been successfully demonstrated as a faster and simpler way to realize feedback control. Furthermore, precalculation of controller gains reduce required computational power for embedded control; one might imagine a small set of desired

deflection points for a particular set-and-hold application, and associated controller gains precalculated as a look-up table.

5.5. Future Work

Future work may include a number of directions. First and foremost, simulation of feedback in a comprehensive, multi-physics environment is required to fully understand any cross-coupling between the FBMD and control circuitry. Second, and perhaps in lieu of such an environment, an experiment may be set up such that a deflected beam be steered to a distance that would require FBMD deflection of more than one-third of the gap. A modern, commercial microcontroller may well be able to read voltage across the FBMD, source a small current, and implement in real-time the precalculated control law presented in Chapter 4.

The LQ control law may be extended to a command generated tracker (CGT) control law, with which the deflection may follow a trajectory more complicated than a simple set-and-hold. With CGT control, the FBMD may be capable of “painting,” or tracking, a target in real-time, rather than discrete pointing control. Other types of MEMS actuation may be considered as well, such as electrothermal or microfluidic. Controller development for other phenomena would proceed in much the same way: by describing the basic physics, analyzing the system for deviations, creating a model, and translating that model into state space. The more precise the model, the higher performance the KF is capable of achieving.

Appendix

```
%Start main script
%Physical Constant declaration
Rint=1e6; %source resistance
e0=8.854187817e-12; %free space permittivity
a=1e-8./4; %effective plate area, accounting for fringe fields
e0A=e0.*a;
m=4.66e-11./4; %calculated plate mass
ks=15.059./4; %simulated effective spring constant
g0=2e-6; %initial gap space
b=1.1885e-5; %fluid damping coefficient
Vpi=sqrt((8.*ks.*g0.^3)./(27.*e0A)); %analytical pull-in voltage
tc=sqrt(m./ks); %system time constant
dt=50e-9; %nanosecond samples, 1GHz DAq
t_last=2500e-6;
t=0:dt:t_last;
sam_last=length(t);

%Filter Model parameters
q1=1e-2;
q2=1e-8;
q3=1;
Rw=0.06;
R = (Rw); % Measurement noise covariance
Q = [q1 0 0;0 q2 0;0 0 q3]; % Dynamics noise strength

%Mapping
H = [1 0 0];
C = [0 1 0];

%Initialize model state and control signal
yd=9.6996e-8;%1e-6;
u0=(g0-yd).*sqrt((2.*ks.*yd)./(e0A.*Rint.^2));
x0=[u0.*Rint;yd;0];

% Discretize state dynamics matrix using Jacobian
F=[(x0(2)-g0)./(Rint.*e0A) (x0(1)-u0.*Rint)./(Rint.*e0A) 0;
  0 0 1;
  e0A.*x0(1).*(g0-x0(2)).^-2./m -ks./m+e0A.*x0(1).^2.*(g0-
  x0(2)).^-3./m - b./m];
B=[(g0-x0(2))./e0A;0;0];
G=eye(3);
[phi, Bd ,Qd]=equiv_discrete(F,B,G,Q,dt); %EENG 765,Lt Col Vazquez
Gd=eye(3);
Pi=inv([phi-eye(3),Bd;C,0]);
Gc=getGc(phi,Bd,u0); %Get LQ gains
Kx=Gc(1:3)*Pi(1:3,1:3)+Gc(4)*Pi(4,1:3); %Calc prop. gain
Kxi=Gc(1:3)*Pi(1:3,4)+Gc(4)*Pi(4,4); %Calc pseudo-rate gain
```



```

%Preloads for speed
x=zeros(3,sam_last);
P=zeros(3,3,sam_last);
z=zeros(2,sam_last);
u=zeros(1,sam_last);
A=zeros(1,sam_last);
sigma_f=zeros(3,sam_last);
residual=zeros(1,sam_last);
e=zeros(2,sam_last);

% Filter Initial conditions
x(:,1)=[1e-15 1e-15 1e-15];
u(1)=Kxi*(yd-C*x(:,1)); %Initial control signal assuming u0=0 and x
steady state
P(:, :, 1)=eye(3).*1e1;

% Kalman filter
for k=2:sam_last
    % Propagate
    x(:,k)= phi*x(:,(k-1))+Bd*u(k-1);
    P(:, :, k)= phi*P(:, :, (k-1))*phi'+Gd*Qd*Gd';

    % Update
    A(:,k)= H*P(:, :, k)*H' + R;
    K=P(:, :, k)*H'*(A(:,k)^-1);
    z(:,k)=get_meas((k-1).*dt,k.*dt,[z(1,(k-1)),z(2,(k-1)),0],u(k-
1));%(t0,tf,x0,u);
    residual(:,k)=z(1,k)-H*x(:,k);
    x(:,k)=x(:,k)+K*residual(:,k); %(3x1)+(3x1)*(1x1)
    u(k)=u(k-1)-Kx*(x(:,k)-x(:,k-1))+Kxi*(yd-C*x(:,k-1));
    P(:, :, k)=P(:, :, k)-K*H*P(:, :, k);
    sigma_f(:,k)=sqrt(diag(P(:, :, k)));
end % End time loop

% Compute error states
e=geterr(t,x(1,:),x(2,:),u); %Generate truth from FEM data

% Compute statistics of the error states and plot
figure(1)
for j=1:2
    subplot(2,1,j);
    plot(t,e(j,:),t,2*sigma_f(j,:), 'r--',t,-2*sigma_f(j,:), 'r--')
end
figure(1),subplot(211);grid on
title(['State Error and Uncertainty (2\sigma)'])
ylabel('Voltage');
subplot(212);ylabel('Gap');grid on

```

```

figure(2)
plot(t,residual,'o-',t,2.*sqrt(A),'r--',t,-2.*sqrt(A),'r--')
title(['Residual and Uncertainty (2\sigma)'])
end

function [Gc] = getGc(phi,Bd,u0)
phia=[phi Bd;0 0 0 1];
Bda=[zeros(3,1);1];
%should be incremental!
X11=[0.0025 0 0;0 2.5e11 0;0 0 1];%3e3]; %max V=20 g=2e-6 v=0.0185
X12=zeros(3,1);
X22=1./(0.2.*u0).^2;
Xcost=[X11 X12;X12' X22];
Ucost=1e3;%1e4; %assume source max 10mA
S=zeros(4,1);
%S=[1;0;0];
%E=eye(2); %same dimension as Bd
%[Kc,L,Gc,report] = dare(phi,Bd,Xcost,Ucost)
[Gc,S,E]=dlqr(phia,Bda,Xcost,Ucost,S)
end

function out = get_meas(t0,tf,x0,u)
%calculates analytical solution of state dynamics given start time
t0,
%stop time tf, previously analytically calc'd state as initial
condition
%x0, and control input u
%Output is [voltage, gap]
[t,y]=ode45(@potent,[t0 tf],x0,[],u);
out=y(size(y,1),1:2)'; %just take the last voltage and gap solutions
%R_nois=0.01.*randn; %emulate +/-10% resistor tolerance
%g_nois=0.1.*randn; %optical sensor error
R_nois=0.1.*rand-.05;
g_nois=0.1.*rand-.05;
out(1,1)=out(1,1).*(1+R_nois); %voltage
out(2,1)=out(2,1).*(1+g_nois); %gap

```

```

function dxdt=potent(t,x,u)
Rint=1e6;%source resistance
e0=8.854187817e-12;
a=1e-8./4;
e0A=e0.*a;
m=4.66e-11./4;
ks=15.059./4;
g0=2e-6;
b=9.4779e-4;
dxdt(3)=0.5.*e0A.*x(1).^2.*(g0-x(2)).^-2./m-b.*x(3)./m-ks.*x(2)./m;
dxdt(2)=x(3);
dxdt(1)=((g0-x(2))./e0A).*(u-x(1)./Rint);
dxdt=dxdt';

```

```

function err=geterr(tobs,Vobs,Dobs,u)
load Icap.mat
load Qfem_CxV.mat
load dispfem.mat
stop=length(tobs);
Qobs=zeros(1,stop);
err=zeros(2,stop);
Qobs(1)=0;
for i=2:stop
Qobs(i)=trapz(tobs(1,1:i),(u-Vobs(1,1:i)./Rint));
for j=2:length(Qfem) %find 1st time Qfem>Qobs
[r,c]=find((Qfem(j).q-Qobs(i))>0,1);
if isempty(r)%find((Qfem(j).q-Qobs(i))>0,1,'first'))
elseif(Qfem(j).q==Qobs(i)) Qflag=1
else %index(1,i)=find((Qfem(i).q-Qobs)<0,1,'last')
index=j;
%output=Qfem(j).v(1);
break
end
end
%err(1,i)=interp1(Qfem(index).q,Qfem(index).v,Qobs,'spline')-Vobs;
%now linearly interpolate between voltages
if(r==1 && index==2) %when Qobs is less than all Qfem data
last=length(Qfem(index-1).v);
m=(Qfem(index).q(r)-0)./(Qfem(index).v(r)-0);
err(1,i)=((Qobs(i)-Qfem(index).q(r)+m.*Qfem(index).v(r))./m)-
Vobs(i);
elseif(r==1 && index>2) %when Qobs is btn discrete FEM steps
last=length(Qfem(index-1).v);
m=(Qfem(index).q(r)-Qfem(index-1).q(last))./(Qfem(index).v(r)-
Qfem(index-1).v(last));
err(1,i)=((Qobs(i)-Qfem(index).q(r)+m.*Qfem(index).v(r))./m)-
Vobs(i);
else %when Qobs falls within an FEM sim
last=r-1;
m=(Qfem(index).q(r)-Qfem(index).q(last))./(Qfem(index).v(r)-
Qfem(index).v(last));
err(1,i)=((Qobs(i)-Qfem(index).q(r)+m.*Qfem(index).v(r))./m)-
Vobs(i);
end
end
%err=Qobs;
for i=1:length(Dispsem)
disp_resam(i).ts=resample(Dispsem(i).ts,tobs);
end
for tau=1:length(tobs) %for each trajectory time tau
for j=1:51 %and each input
gvsv(tau).d(j,2)=disp_resam(j).ts.data(tau);
gvsv(tau).d(j,1)=Qfem(j).v(1);
end
%tau;

```

```
err(2,tau)=interp1(gvsv(tau).d(:,1),gvsv(tau).d(:,2),Vobs(tau),'spline')-Dobs(tau);  
    %errd(tau)=temp(tau)-x(2,tau);  
end  
err(2,tau)=interp1(gvsv(tau).d(:,1),gvsv(tau).d(:,2),Vobs(tau),method,'spline');
```

Bibliography

- [1] K. Al-Arife and G. K. Knopf, "Neural network control of a MEMS torsion micro mirror," *Proc. 2005 IEEE Conf. Control Applications*, Toronto, Canada, Aug. 2005, pp. 737-742.
- [2] N. Arancibia *et al.*, "Adaptive Control of a MEMS Steering Mirror for Suppression of Laser Beam Jitter," *2005 Amer. Control Conf.*, Portland, OR, Jun. 2005, pp. 3586-3591.
- [3] B. Borovic *et al.*, "The lateral instability problem in electrostatic comb drive actuators: modeling and feedback control", *J. Micromech. Microeng.*, pp.1233-1241, 2006.
- [4] B. Borovic *et al.*, "Open-loop versus closed-loop control of MEMS devices: choices and issues," *J. Micromech. Microeng.*, no. 15, pp. 1917-1924, 2005.
- [5] J. Bryzek *et al.*, "Control Issues for MEMS", *Proc. 42nd IEEE Conference on Decision and Control*, Maui, HI, Dec. 2003, pp. 3039-3047.
- [6] D. Burns and V. Bright, "Nonlinear flexures for stable deflection of an electrostatically actuated micromirror," *Proc. SPIE*, pp. 125-136, 1997.
- [7] L. Castañer *et al.*, "Analysis of the extended operation range of electrostatic actuators by current-pulse drive," *Sensors and Actuators A*, pp. 181-190, 2001.
- [8] E. Chan and R. W. Dutton, "Electrostatic Micromechanical Actuator with Extended Range of Travel," *J. Microelectromech. Syst.*, vol. 9, no. 3, pp. 321-328, Sep. 2000.
- [9] P. Cheung *et al.*, "Identification, Position Sensing, and Control of an Electrostatically-driven Polysilicon Microactuator," in *Proc. 34th Conf. Decision & Control*, New Orleans, LA, 1995, pp. 3545-3550.
- [10] P. B. Chu and K. S. J. Pister, "Analysis of Closed-loop Control of Parallel-Plate Electrostatic MicroGrippers," in *IEEE Int. Conf. Robotics and Automation*, San Diego, CA, 1994, pp. 820-825.
- [11] W. Cowan, "Foundry Microfabrication of Deformable Mirrors for Adaptive Optics," Ph.D. dissertation, Dept. Elect. and Comp. Eng., Air Force Inst. Tech., WPAFB, OH, 1998.
- [12] M. F. Daqaq *et al.*, "Input-shaping control of nonlinear MEMS," *Nonlinear Dynamics*, 2007 © Springer. doi: 10.1007/s11071-007-9246-x

- [13] H. J. Hall, "Control and Characterization of Line-Addressable Micromirror Arrays," M.S. Thesis, Dept. Elect. and Comp. Eng., Air Force Inst. Tech., WPAFB, OH, 2001.
- [14] E. S. Hung and S. D. Senturia, "Extending the Travel Range of Analog-Tuned Electrostatic Actuators," *J. Microelectromech. Syst.*, vol. 8, no. 4, pp. 497-505, Dec. 1999.
- [15] A. Izadian *et al.*, "Adaptive Control of MEMS Devices," *Proc. IASTED Int. Conf. Intelligent Syst. and Control*, Honolulu, HI, 2006, pp. 107-112.
- [16] C. Kharrat *et al.*, "Microbeam dynamic shaping by closed-loop electrostatic actuation using modal control," *Research in Microelectronics and Electronics Conf.*, Bordeaux, FR, 2007, pp. 197-200.
- [17] J. M. Kyynäräinen *et al.*, "Increasing the Dynamic Range of a Micromechanical Moving-Plate Capacitor," *Analog Integrated Circuits and Signal Processing*, no. 29, pp. 61-70, 2001.
- [18] E. Lemaire *et al.*, "Topology optimization of electromechanical microsystems against pull-in voltage," *7th Int. Conf. on Thermal, Mechanical, and Multiphysics Simulations and Experiments in Micro-Electronics and Micro-Systems*, Como, Italy, Apr. 2006, pp. 1-8.
- [19] K. Liao *et al.*, "Closed-loop adaptive control for electrostatically driven torsional micromirrors," *J. Microlith., Microfab., Microsyst.*, vol. 4, no. 4, pp. 041503-1-9, 2005.
- [20] S. E. Lyshevski, "Micro-Electromechanical Systems: Motion Control of Micro-Actuators," *Proc. 37th IEEE Conf. Decision & Control*, Tampa, FL, 1998, pp. 4334-4335.
- [21] D. H. S. Maithripala *et al.*, "Capacitive Stabilization of an Electrostatic Actuator: An Output Feedback Viewpoint," *Proc. Amer. Control Conf.*, Denver, CO, 2003, pp. 4053-4058.
- [22] D. H. S. Maithripala *et al.*, "Control of an Electrostatic Microelectromechanical System Using Static and Dynamic Output Feedback," *J. Dynamic Syst., Measurement, and Control*, vol. 127, pp. 443-450, Sep. 2005.
- [23] D. H. S. Maithripala *et al.*, "A General Modeling and Control Framework for Electrostatically-Actuated Mechanical Systems," *Int. J. Robust Nonlinear Control*, pp. 1-19, 2002.
- [24] D. H. S. Maithripala *et al.*, "Integrated Modeling and Control of Electrostatic MEMS, Part II: Control," *Proc. IEEE Int. Conf. Inform. and Automation*, Colombo, Sri Lanka, 2005, pp. 424-428.

- [25] D. H. S. Maithripala *et al.*, "Nano-precision control of micromirrors using output feedback," *Proc. 42nd IEEE Conf. Decision and Control*, Maui, HI 2003, pp. 2652-2657.
- [26] D. H. S. Maithripala *et al.*, "Nonlinear Dynamic Output Feedback Stabilization of Electrostatically Actuated MEMS," *Proc. 42nd Conf. Decision and Control*, Maui, HI, 2003, pp. 61-66.
- [27] L. Mol *et al.*, "Full-Gap Positioning of Parallel-Plate Electrostatic MEMS Using On-off Control," *IEEE Int. Symp. Industrial Electronics*, Vigo, Spain, 2007, pp. 1464-1468.
- [28] R. Nadal-Guardia *et al.*, "Current drive methods to extend the range of travel of electrostatic microactuators beyond the voltage pull-in point," *J. Microelectromech. Syst.*, vol. 11, no. 3, pp. 255-263, Jun 2002.
- [29] K. Nonaka *et al.*, "Bi-directional Extension of the Travel Range of Electrostatic Actuators by Open Loop Periodically Switched Oscillatory Control," *43rd IEEE Conf. Decision and Control*, Atlantis, Bahamas, 2004, pp. 1964-1969.
- [30] K. O. Owusu, "Nonlinear Control of Microelectromechanical Systems (MEMS) Devices," M.S. Thesis, Dept. Elect. Eng., Univ. Texas at Arlington, Arlington, TX, 2006.
- [31] G. A. Peterson, "Control Demonstration of a Thin Deformable In-Plane Actuated Mirror," M.S. Thesis, Dept. Elect. and Comp. Eng., Air Force Inst. Tech., WPAFB, OH, 2006.
- [32] D. Piyabongkarn *et al.*, "Travel Extension of a MEMS Electrostatic Microactuator," *IEEE Trans. Control Syst. Technology*, vol. 13, no. 1, Jan 2005, pp. 138-145.
- [33] D. Qiao *et al.*, "A two-beam method for extending the working range of electrostatic parallel-plate micro-actuators," *J. Electrostatics*, no. 65, pp. 256-262, Oct. 2006.
- [34] L. A. Rocha *et al.*, "Using Dynamic Voltage Drive in a Parallel-Plate Electrostatic Actuator for Full-Gap Travel Range and Positioning," *J. Microelectromech. Syst.*, vol. 15, no. 1, Feb 2006, pp. 69-83.
- [35] P. C. Rounsavall, "Modulation of Electrostatic Microelectromechanical Mirrors Using a CMOS Controller," M.S. Thesis, Dept. Elect. and Comp. Eng., Air Force Inst. Tech., WPAFB, OH, 1999.
- [36] H. S. Sane *et al.*, "Application of Sliding Mode Control to Electrostatically Actuated Two-Axis Gimbaled Micromirrors," *Proc. Amer. Control Conf.*, Denver, CO, 2003, pp. 3726-3731.

- [37] J. I. Seeger and S. B. Crary, "Stabilization of Electrostatically Actuated Mechanical Devices," *Transducers '97, 1997 Int. Conf. Solid-State Sensors and Actuators*, Chicago, IL, 1997, pp. 1133-1136.
- [38] J. I. Seeger and S. B. Crary, "Analysis and simulation of MOS capacitor feedback for stabilizing electrostatically actuated mechanical devices," *2nd Int. Conf. Simulation and Design of Microsyst. and Microstructures*, Lausanne, Switzerland, Sep. 1997, pp. 199-208.
- [39] J. I. Seeger and B. E. Boser, "Dynamics and Control of Parallel-Plate Actuators Beyond the Electrostatic Instability," *Transducers '99, 10th Int. Conf. Solid-State Sensors and Actuators*, Sendai, Japan, 1999, pp. 474-477.
- [40] J. I. Seeger and B. E. Boser, "Charge Control of Parallel-Plate, Electrostatic Actuators and the Tip-In Instability," *J. Microelectromech. Syst.*, vol. 12, no. 5, pp. 656-671 Oct. 2003.
- [41] Y. Sun *et al.*, "A high-aspect-ratio two-axis electrostatic microactuator with extended travel range," *Sensors and Actuators A*, no. 102, pp. 49-60, 2002.
- [42] L. Wang, "Modeling and Real-Time Feedback Control of MEMS Device," Ph.D. Dissertation, Coll. Eng. And Mineral Resources, WV Univ., 2004.
- [43] Y. Zhao *et al.*, "Fast and precise positioning of electrostatically actuated dual-axis micromirror by multi-loop digital control," *Sensors and Actuators A*, no. 132, pp. 421-428, 2006.
- [44] G. Zhu *et al.*, "Improving the Performace of an Electrostatically Actuated MEMS by Nonlinear Control: Some Advances and Comparisons," *Proc. 44th IEEE Conf. Decision and Control*, Seville, Spain, 2005, pp. 7534-7539.
- [45] G. Zhu *et al.*, "On the Differential Flatness and Control of Electrostatically Actuated MEMS," *2005 Amer. Control Conf.*, Portland, OR, 2005, pp. 2493-2498.
- [46] G. Zhu *et al.*, "Flatness-Based Control of Electrostatically Actuated MEMS With Application to Adaptive Optics: A Simulation Study," *J. Microelectromech. Syst.*, vol. 15, no. 5, pp. 1165-1174, Oct 2006.
- [47] G. Zhu *et al.*, "Robust Control of an Electrostatically Actuated MEMS in the Presence of Parasitics and Parametric Uncertainties," *Proc. 2006 Amer. Control Conf.*, Minneapolis, MN, 2006, pp. 1233-1238.
- [48] G. Zhu *et al.*, "Robust Output Feedback Control of an Electrostatic Micro-Actuator," *Proc. 2007 Amer. Control Conf.*, New York City, NY 2007, pp. 3192-3197.

- [49] G. Zhu and J. Lévine, "Stabilization of an Electrostatic MEMS Including Uncontrollable Linearization," *Proc. 46th IEEE Conf. Decision and Control*, New Orleans, LA, 2007, pp. 2433-2438.
- [50] M. Bao *et al.*, "Modified Reynolds' equation and analytical analysis of squeeze-film air damping of perforated structures," *J. Micromech. Microeng.*, vol. 13, pp. 795-800, 2003.
- [51] M. Bao and H. Yang, "Squeeze film air damping in MEMS," *Sensors and Actuators A*, no. 136, pp. 3-27, Jan. 2007.
- [52] J. Jang and S. T. Wereley, "Effective heights and tangential momentum accommodation coefficients of gaseous slip flows in deep reactive ion etching rectangular microchannels," *J. Micromech. Microeng.*, vol. 16, pp. 493-504, Jan. 2006.
- [53] W. Li, "Analytical modelling of ultra-thin gas squeeze film," *Nanotechnology*, no. 10, pp. 440-446, Sep. 1999.
- [54] Y. Mitsuya *et al.*, "Averaged Reynolds Equation Extended to Gas Lubrication Possessing Surface Roughness in the Slip Flow Regime: Approximate Method and Confirmation Experiments," *J. Tribology*, vol. 111, pp. 495-503, Jul. 1989.
- [55] R. Pratap *et al.*, "Squeeze Film Effects in MEMS Devices," *J. Indian Inst. Science*, vol. 87, no. 1, pp. 75-94, Mar. 2007.
- [56] J. B. Starr, "Squeeze-Film Damping in Solid-State Accelerometers," in *Solid-State Sensor and Actuator Workshop*, pp. 44-47, Jun. 1990.
- [57] T. Veijola *et al.*, "Equivalent-circuit model of the squeezed gas film in a silicon accelerometer," *Sensors and Actuators A*, no. 48, pp. 239-248, Jan. 1995.
- [58] T. Veijola *et al.*, "The influence of gas-surface interaction on gas-film damping in a silicon accelerometer," *Sensors and Actuators A*, no. 66, pp. 83-92, 1998.
- [59] T. Veijola, "Compact models for squeezed-film dampers with inertial and rarefied gas effects," *J. Micromech. Microeng.*, vol. 14, pp. 1109-1118, Jun. 2004.
- [60] P. S. Maybeck, "Stochastic processes and linear dynamic system models," in *Stochastic Models, Estimation, and Control Volume 1* (Mathematics in Science and Engineering, vol. 141-1), Springfield, VA: Navtech Book and Software Store, 1994, pp. 133-194.
- [61] P. S. Maybeck, "Design and performance analysis of Kalman Filters," in *Stochastic Models, Estimation, and Control Volume 1* (Mathematics in Science and Engineering, vol. 141-1), Springfield, VA: Navtech Book and Software Store, 1994, pp. 289-350.

- [62] P. S. Maybeck, "Nonlinear stochastic controllers," in *Stochastic Models, Estimation, and Control Volume 3* (Mathematics in Science and Engineering, vol. 141-3), New York, NY: Academic Press, 1982, pp. 223-244.
- [63] J. A. Pelesko and D. H. Bernstein, "Modeling Electrostatic-Elastic Systems," in *Modeling MEMS and NEMS*, Boca Raton, FL: Chapman & Hall/CRC, 2003, pp. 213-256.
- [64] O. Degani *et al.*, "Pull-In Study of an Electrostatic Torsion Microactuator," *J. Micromech. Microeng.*, vol. 7, pp. 373-379, Dec. 1998.
- [65] "ARI MEMS Micromirror Demonstration Devices." Internet: <http://www.adriaticresearch.org/demos.htm>, Nov 20, 2011.
- [66] J. Carter *et al.* (2005, Aug 10). *PolyMUMPs Design Handbook*. [On-line]. Vol 11. Available: http://www.memscapinc.com/__data/assets/pdf_file/0019/1729/PolyMUMPs.DR.11.pdf [Aug 2007].
- [67] "PolyMUMPs FAQ." Internet: http://www.memscapinc.com/__data/assets/pdf_file/0012/1731/PolyMUMPs.faq.v2.pdf, [Nov 20, 2011].
- [68] J. Butler, "Development and Packaging of Microsystems Using Foundry Services," Ph.D. dissertation, Dept. Elect. and Comp. Eng., Air Force Inst. Tech., WPAFB, OH, 1998.
- [69] M. H. Sadd and A. K. Stiffler, "Squeeze Film Dampers: Amplitude Effects at Low Squeeze Numbers." *J. Eng Ind.*, Trans. ASME, vol. 97, Series B, pp. 1366-1370, Nov 1975.
- [70] R. Gupta, "Electrostatic Pull-In Test Structure Design for *In-Situ* Mechanical Property Measurements of Microelectromechanical System (MEMS)," Ph.D. dissertation, Dept. Elect. and Comp. Sci., Massachusetts Inst. Of Tech., Cambridge, MA, 1997.
- [71] V. Leus and D. Elata, "Fringing Field Effect in Electrostatic Actuators," Technion, Israel Inst. Tech., Tech Rep. ETR-2004-2, May 2004.

REPORT DOCUMENTATION PAGE

*Form Approved
OMB No. 074-0188*

The public reporting burden for this collection of information is estimated to average 1 hour per response, including the time for reviewing instructions, searching existing data sources, gathering and maintaining the data needed, and completing and reviewing the collection of information. Send comments regarding this burden estimate or any other aspect of the collection of information, including suggestions for reducing this burden to Department of Defense, Washington Headquarters Services, Directorate for Information Operations and Reports (0704-0188), 1215 Jefferson Davis Highway, Suite 1204, Arlington, VA 22202-4302. Respondents should be aware that notwithstanding any other provision of law, no person shall be subject to a penalty for failing to comply with a collection of information if it does not display a currently valid OMB control number.

PLEASE DO NOT RETURN YOUR FORM TO THE ABOVE ADDRESS.

1. REPORT DATE (DD-MM-YYYY) 22-12-2011		2. REPORT TYPE Master's Thesis		3. DATES COVERED (From – To) 26 Sep 2005-22 Dec 2011	
4. TITLE AND SUBTITLE Linear-Quadratic Control of a MEMS Micromirror using Kalman Filtering				5a. CONTRACT NUMBER	
				5b. GRANT NUMBER	
				5c. PROGRAM ELEMENT NUMBER	
6. AUTHOR(S) Schnapp, Jamie P., Capt				5d. PROJECT NUMBER	
				5e. TASK NUMBER	
				5f. WORK UNIT NUMBER	
7. PERFORMING ORGANIZATION NAMES(S) AND ADDRESS(S) Air Force Institute of Technology Graduate School of Engineering and Management (AFIT/EN) 2950 Hobson Way Wright-Patterson AFB OH 45433-7765				8. PERFORMING ORGANIZATION REPORT NUMBER AFIT/GE/ENG/11-44	
9. SPONSORING/MONITORING AGENCY NAME(S) AND ADDRESS(ES) Intentionally Left Blank				10. SPONSOR/MONITOR'S ACRONYM(S) N/A	
				11. SPONSOR/MONITOR'S REPORT NUMBER(S)	
12. DISTRIBUTION/AVAILABILITY STATEMENT Distribution A. Approved for Public Release; Distribution Unlimited					
13. SUPPLEMENTARY NOTES This material is declared a work of the U.S. Government and is not subject to copyright protection in the United States.					
14. ABSTRACT The deflection limitations of electrostatic flexure-beam actuators are well known. Specifically, as the beam is actuated and the gap traversed, the restoring force necessary for equilibrium increases proportionally with the displacement to first order, while the electrostatic actuating force increases with the inverse square of the gap. Equilibrium, and thus stable open-loop voltage control, ceases at one-third the total gap distance, leading to actuator snap-in. A Kalman Filter is designed with an appropriately complex state dynamics model to accurately estimate actuator deflection given voltage input and capacitance measurements, which are then used by a Linear Quadratic controller to generate a closed-loop voltage control signal. The constraints of the latter are designed to maximize stable control over the entire gap. The design and simulation of the Kalman Filter and controller are presented and discussed, with static and dynamic responses analyzed, as applied to basic, 100 μm by 100 μm square, flexure-beam-actuated micromirrors fabricated by PolyMUMPs. Successful application of these techniques enables demonstration of smooth, stable deflections of 50% and 75% of the gap.					
15. SUBJECT TERMS MEMS micromirror, linear-quadratic control, kalman filter, electrostatic actuation, deflection stabilization					
16. SECURITY CLASSIFICATION OF:			17. LIMITATION OF ABSTRACT UU	18. NUMBER OF PAGES 90	19a. NAME OF RESPONSIBLE PERSON Dr. Ronald Coutu
REPORT U	ABSTRACT U	c. THIS PAGE U			19b. TELEPHONE NUMBER (Include area code) (937) 255-3636 x7230 ronald.coutu@afit.edu